Nanoscale Advances

ROYAL SOCIETY OF CHEMISTRY

REVIEW

View Article Online
View Journal

Cite this: DOI: 10.1039/d5na01137j

SERS and SEF with enhancement in nanogaps: from fabrication to biosensing

Alisher Sultangaziyev, Dinmukhamed Aliyev, Ansar Seitkali and Rostislav Bukasov *

This review surveys SERS and SEF spectroscopies, with a spotlight on the correlation between nanogap fabrication techniques and subsequent applications of those nanogaps in biosensing. In the last several decades, the development of new nanofabrication techniques and novel applications substantially increased the importance of these spectroscopic techniques for biosensing. The cornerstone of this development is the application and control of nanogaps between nanoparticles and nanostructures. Nanogaps are important since they may be responsible for the biggest portion of signal enhancement in SERS and SEF. This review summarizes and provides insights into the theory behind nanogap enhancement, nanogap fabrication, and its applications in direct and indirect biosensing. The theoretical part includes studies on the origin of nanogap enhancement and its dependence on gap distance and agglomeration. Next, the review presents and compares structured and unstructured fabrication techniques with a few dozen examples tabulated with their figures of merit, like the enhancement factor (EF) and limit of detection (LOD). In total, 50 SERS-based and 26 SEF-based articles were tabulated, whereas 38 papers were classified based on the synthesis method and based on the EF and median LOD values calculated for Electron Beam Lithography (EBL) and Template-Assisted (TA) prepared substrates that were no more than one order of magnitude better or about the same as those for other fabrication methods (median 1×10^{-10} and 8×10^{-10} M for EBL and TA, respectively, *vs.* median 4×10^{-8} and 1×10^{-9} M for nanosphere lithography (NSL) and Self-Assembly (SA), respectively). The median EF for substrates fabricated with EBL, NSL, and TA methods (4.6×10^{8}, 1.0×10^{8}, and 1.4×10^{8}) demonstrates only a moderate advantage over the SA technique, with a median EF of 0.3×10^{8}. However, unstructured nanofabrication techniques like self-assembly have a more affordable price, lower complexity, and better scalability. Therefore, SA can easily compete with ordered nanofabrication techniques. In addition, this review also highlights the applications of nanogaps in label-free detection and biomarker detection. Finally, this review highlights applications of nanogap enhancement in SEF and draws conclusions on the current state of nanogap research and its future.

Received 16th December 2025
Accepted 20th March 2026

DOI: 10.1039/d5na01137j

rsc.li/nanoscale-advances

Introduction

The first observation of surface-enhanced spectroscopy was made almost 50 years ago by Fleischmann *et al.* while recording Raman spectra of pyridine adsorbed on a roughened silver substrate.[1] In the following years, this phenomenon was explained by two groups independently, Jeanmaire and van Duyne with the electromagnetic effect and Albrecht and Creighton with the charge-transfer effect.[2,3] These hypotheses evolved into currently accepted two mechanisms of Raman signal enhancement: electromagnetic enhancement and chemical enhancement. The relationship between the normal Raman signal and the SERS signal can be seen in the equation below, where P_{SERS} and P_{Raman} represent respective signal intensities and G_{SERS} denotes a combination of electromagnetic and chemical enhancements.

$$P_{SERS} = G_{SERS}P_{Raman} = G_{SERS}^{Em}G_{SERS}^{Chem}P_{Raman} \quad (1)$$

Electromagnetic enhancement arises from the light-induced electric fields on the surface of particular nanostructures. These enhanced electric fields are generated when the incident light is in resonance with the oscillations of conduction electrons of the metal nanoparticle, which will make conduction electrons oscillate collectively. This optical phenomenon is called localized surface plasmon resonance (LSPR).[4] Electromagnetic enhancement increases the Raman scattering at least by a factor of 10^4 and as high as 10^{10}.[5,6] This enhancement mechanism depends mostly on the configuration of the substrate, though the polarization and orientation of the analyte molecule also have an effect. It can be seen more clearly in eqn (2) for the

Department of Chemistry, School of Sciences and Humanities (SSH), Nazarbayev University, Astana, Kazakhstan. E-mail: rostislav.bukasov@nu.edu.kz

!"tx1#count(//biography)"^?^(4)single-molecule electromagnetic enhancement $|E^4|$ approximation, where $M^Z_{\mathrm{Loc}}(\omega_{\mathrm{L}})$ and $M^Z_{\mathrm{Loc}}(\omega_{\mathrm{R}})$ are the terms for the field enhancement generated by laser polarization at the laser frequency and Raman frequency.[7] It should be noted that while $|E^4|$ approximation is a commonly used simplification, it does not provide an accurate description of all SERS cases. Specifically, it might fail in situations involving strong molecule–metal surface coupling and in cases where chemical enhancement makes a significant contribution to the overall Raman signal.

$$G^{\mathrm{EM}}_{\mathrm{SERS}}(E^4) = M^Z_{\mathrm{Loc}}(\omega_{\mathrm{L}})M^Z_{\mathrm{Loc}}(\omega_R) = \left[\frac{E_{\mathrm{Loc}}(\omega_{\mathrm{L}})}{E(\omega_{\mathrm{L}})}\right]^2\left[\frac{E_{\mathrm{Loc}}(\omega_{\mathrm{R}})}{E(\omega_{\mathrm{R}})}\right]^2 \quad (2)$$

On the other hand, chemical enhancement arises from localized electronic resonances of the adsorbate or charge-transfer resonances between the adsorbate and the metal surface, leading to enhancement factors on the order of 100.[8] This phenomenon can be further explained by the following equation, where σ_k^{ads} and σ_k^{free} represent the k-th order vibrational mode Raman frequencies of the free and adsorbed molecules.

$$G^{\mathrm{Chem}}_{\mathrm{SERS}} = \sigma_k^{\mathrm{ads}}/\sigma_k^{\mathrm{free}} \quad (3)$$

The combination of these two phenomena can produce signal enhancement levels as high as 10^{14} orders of magnitude.[9]

In addition to high sensitivity due to the high enhancement, non-destructive nature for some applications (like TERS),

Alisher Sultangaziyev

Alisher Sultangaziyev earned his BSc (2019) and MSc (2021) in Chemistry from Nazarbayev University, where he conducted research as a member of Professor Bukasov's group. He is currently pursuing his PhD at the Ulsan National Institute of Science and Technology (UNIST), Republic of Korea, and is a graduate researcher in Professor Rodney S. Ruoff's group at the Center for Multidimensional Carbon Materials (CMCM), Institute for Basic Science (IBS). His research interests center on carbon materials synthesis and processing, CVD diamond growth, and advanced characterization techniques based on Raman spectroscopy.

Dinmukhamed Aliyev

Aliyev Dinmukhamed is currently an MSc student at Nazarbayev University in Kazakhstan. He received his BSc in Chemistry from KAIST, where he conducted his undergraduate research under the supervision of Professor Kiyoung Park. Later he worked in Dr Bukasov's lab. He is also currently working as a Project Manager at Inospin, supporting research and innovation projects at the interface of academia and industry.

Ansar Seitkali

Ansar Seitkali is currently a junior BSc Chemistry student at Nazarbayev University (Astana, Kazakhstan). He is currently working as a research assistant at the Surface-Enhanced Spectroscopy & Biodetection Lab under the supervision of Associate Professor Rostislav Bukasov. His research interests focus on analytical chemistry.

Rostislav Bukasov

Dr. Rostislav Bukasov graduated from Kharkiv NU in 1994, owned a small photoservice business, worked as analytical chemist for one year, came to the U of Utah, SLC, earned a PhD in analytical chemistry as the most cited PhD student in the 2004 class, has 1st author publications in Nano Letters, ACS Nano, *and* Analytical Chemistry, *supervised by professor Shumaker Parry, worked at the Nanoinstitute of Utah for Marc Porter, and moved to Kazakhstan in 2012 to work as assistant professor of analytical chemistry at Nazarbayev University. He is happily married, a father of 5 surviving children, and a climber of Peak Lenina (7134 m) and has traveled to 87 countries and 408 UNESCO WHSs.*

relatively high speed of analysis, and the ability for label-free detection, SERS has strong potential for multiplexing, since it has relatively narrow Raman peaks in the spectrum, where dozens of different Raman peaks can be resolved.[10] Because of these and other advantages, SERS has found applications in molecular biology,[11–13] biomedicine,[14–16] and environmental science,[17] showcasing even single-molecule detection.[18–21] This increase in popularity led to the development of other surface-enhanced spectroscopies, like surface-enhanced fluorescence (SEF).

Fluorescence spectroscopy has been an indispensable analytical instrument in biotechnology and medicine over the last 40 years. It detects molecules with moderate to high sensitivity quickly and reliably.[22] Nonetheless, improving the sensitivity of this technique is still highly desirable. This property of fluorescence is usually limited by the quantum yield and fluorescence lifetime. The quantum yield (Q_0) determines the efficiency of the fluorescence and demonstrates the ratio of photon emission against non-radiative decay:

$$Q_0 = \frac{\Gamma}{\Gamma + k_{nr} + k_q} \quad (4)$$

where Γ is the radiative decay rate of the fluorophore, which is the rate of photon emission. The terms k_{nr} and k_q depict the phenomena by which the fluorophore can return to the ground state: non-radiative decay and other quenching processes, respectively. The fluorescence lifetime is described by the time the fluorophore remains in the first singlet state on the Jablonski diagram[23] and illustrated by the following equation:

$$\tau_0 = \frac{1}{\Gamma + k_{nr} + k_q} \quad (5)$$

Usually, these parameters can be altered by changing the magnitude of the non-radiative decay and other quenching processes, as the radiative decay rate Γ is the constant value that depends on the extinction coefficient of the fluorophore.[24] However, by placing the fluorophore near the conducting metal surface or particle, it is possible to change the radiative decay rate Γ and influence the quantum yield and fluorescence lifetime.[25]

The theoretical background behind the effects of metal surfaces on fluorescence has been well studied and summarized in various articles and reviews.[26–28] It was found that two main effects are responsible for the change in the fluorescence in the proximity of the metal surface. The first one is the amplification of the incident light by the inner free electrons of the metal, which is called the "lightning rod effect".[29] This effect can be utilized to obtain localized enhancement of the fluorescence and to significantly increase the rate of excitation and intensity. It should be noted, however, that the lightning rod effect is not completely independent of localized surface plasmon resonance, but rather represents an engineering (geometrical) contribution to EM enhancement mechanisms. The second effect is the increase in the radiative decay rate through the additional metal-induced radiative rate Γ_m. This term modifies eqn (4) and (5) accordingly:

$$Q_m = \frac{\Gamma + \Gamma_m}{\Gamma + \Gamma_m + k_{nr} + k_q} \quad (6)$$

$$\tau_m = \frac{1}{\Gamma + \Gamma_m + k_{nr} + k_q} \quad (7)$$

So, an increase in quantum yield and a decrease in fluorescence lifetime can be achieved by placing the fluorophore near the conducting metal surface or particle. The combination of these phenomena is called metal-enhanced fluorescence (MEF) or, more broadly, surface-enhanced fluorescence.[30,31]

The main sources of signal enhancement in surface-enhanced spectroscopies are "hot spots", which are mainly spatial regions with a high density of electromagnetic field enhancement. These enhanced EM regions increase the radiative emission rate and field strengths and subsequently produce significant signal enhancement.[20,32] These regions are mostly on the tips of nanostructures or in nanogaps between nanoparticles.[33] The highest enhancement levels are mostly observed in nanostructures containing sufficiently small nanogaps, with enhancement increasing dramatically near the 1 nm mark.[34,35] Those small nanogaps are more efficient due to the increase in the electric field and amplification of light polarization.[36] Thus, the use of systems containing nanogaps is highly preferred in order to achieve the best sensitivity. As an example, some of the first successful studies on single-molecule detection involved nanogaps from ensembles of aggregated metal nanoparticles.[34,35] However, obtaining nanostructures with reproducible high enhancement factors is the biggest challenge for these spectroscopic techniques.[37,38] In this review, we will start with a brief explanation of the nanogap phenomenon and then present and discuss the design and synthesis of highly structured and unstructured plasmonic nanogap structures for spectroscopic applications. Then, we will provide examples for applications of these nanogap structures for sensing and detection of different analytes and biomarkers. Finally, we will discuss recent progress in SEF applications on nanogap-based substrates.

Nanogap enhancement in aggregated nanostructures

It is well known that the highest signal enhancement is observed in nanogap hot spots.[7] So, research on the theory behind this phenomenon through simulations and experiments is essential for the development of surface-enhanced spectroscopies. The understanding of this phenomenon will help design more efficient plasmonic nanostructures with better enhancement capabilities, which can be applicable for different applications. This chapter will be dedicated to the theory of hotspots in nanogaps.

Origin of nanogap enhancement

The reason why very strong fields are generated inside small gaps can be inferred by looking at Fig. 1, which illustrates the

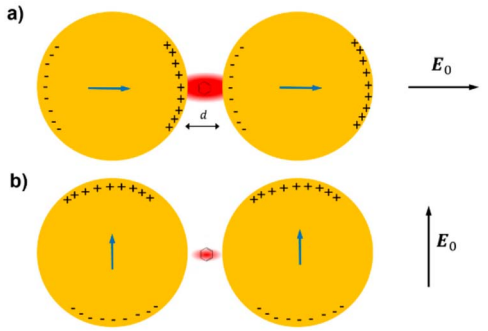

Fig. 1 A dimer formed by two nanoparticles, separated by a gap g, is polarized by the action of an external electric field E_0: (a) along the main axis and (b) perpendicular to the main axis. Reproduced under Creative Commons License from an open-access Pilot *et al.* 2019 article.[7]

case of a molecule placed in between two metallic spheres; in panel (a) the electric field is polarized along the main axis of the dimer, while in panel (b) it is polarized perpendicularly to the axis; the electric field polarizes the nanoparticles, inducing time-oscillating positive and negative surface charge densities on opposite sides of the nanoparticles themselves.[36] In the on-axis polarization, one can observe that bringing nanoparticles close to each other reduces the separation between regions of induced oscillating surface charges and, therefore, increases the electric field in between them. Moreover, the reciprocal interaction between the nanoparticles leads to an increase in their polarizations; in fact, each nanoparticle feels the effect of the external field plus the plasmon-induced polarization response of the nearby nanoparticle. In other words, not only the external field but also the plasmon-induced dipole in one nanoparticle contributes to the polarization of the other nanoparticle. This mutual reinforcement occurs in the configuration shown as (a), where a bonding plasmonic mode is supported. However, in configuration (b) this strong reinforcement is absent due to lack of a bonding plasmon mode that can localize the EM field within the gap.[36]

In addition to the previous qualitative considerations, it is also worth showing a specific case study in which G_{SERS} is numerically calculated for different gap sizes. We shall refer to the work by Le Ru *et al.*, who studied the dimer reported in Fig. 2a.[39] The dimer is formed by two gold nanoparticles with radius $a = 25$ nm immersed in water and separated by a variable gap g. The laser is polarized along the main axis, and the probe molecule is placed at the surface of one of the two nanoparticles, along the main axis. In Fig. 2b and c, the extinction and the enhancement spectra of a single nanoparticle and the dimer (with different gaps) are shown, respectively. The points worth highlighting, especially concerning the local field, are the following. Firstly, G_{SERS} strongly increases by reducing the gap size. It amounts to 5×10^5 at $g = 10$ nm and 3×10^9 at $g = 2$ nm; the power-law dependence is reported to be approximately G_{SERS} $1/g^2$.[40,41] A single gold sphere is limited to 2×10^3. This behavior explains why SERS is very often observed on aggregated nanoparticles and rarely on isolated nanoparticles. There are only very few cases in which aggregation inhibits or weakly enhances Raman scattering; this may occur, for example, with hollow nanoparticles, where aggregation leads to plasmon mode competition and field redistribution between inner and outer surfaces, reducing the field localization in the interparticle gaps.[42] Secondly, for very small gaps ($g < 1$ nm), quantum mechanical phenomena, like electron tunneling, come into play, leading to the saturation of charge-transfer plasmons, limiting the increase in the field enhancement. This subject has been recently studied by Zhu *et al.*[43] and by Hajisalem *et al.*[44]

Thirdly, an important distinction regards the use of a surface-averaged or a single point G_{SERS}: for example, G_{SERS} at $g = 2$ nm, calculated at the intersection of the Z-axis with the surface of one of the nanoparticles, amounts to 3×10^9; if averaged over the surface of the dimer, it is 300 times lower (Fig. 2c dashed line). This suggests that the field is strongly localized in a small spatial region. The local G_{SERS} therefore represents the maximum value at the hot-spot, whereas the surface-averaged G_{SERS} is the quantity more directly relevant to experimentally measured SERS signals.

More insight into the anatomy and properties of hot spots in nanogaps can be obtained by using computational methods like the finite element method (FEM), the finite-difference time-domain (FDTD) method, discrete dipole approximation (DDA), and the generalized multipole Mie (GMM) analysis.[45] For example, the study by Etchegoin *et al.* utilized generalized Mie theory to calculate enhancement factors in a gold nanogap with high accuracy.[46] They found that the average enhancement in the gap region can be almost 300 times lower than the maximum enhancement and most of this signal is coming from only 0.64% of the nanostructure surface. Similar conclusions were derived by McMahon *et al.* with the help of the finite element method.[47] In addition, they found that upon fusion of two gold nanoparticles, the EF in the crevice can go up to 10^{14}.

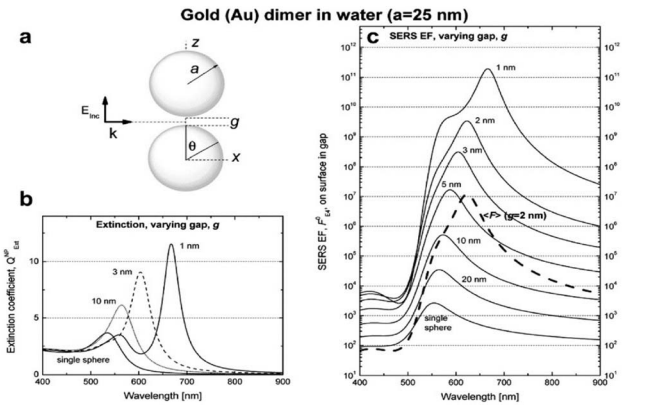

Fig. 2 (a) The dimer under investigation is formed by two gold nanoparticles with radius 'a' and separated by a gap 'g'; the laser is polarized along the main axis. (b) Extinction coefficient for a single sphere and for the dimer (with different gaps) as a function of the wavelength. (c) Continuous lines: SERS enhancement (SERS EF in the figure) for a single sphere and for the dimer (with different gaps) as a function of the wavelength. Reproduced with permission granted by Elsevier B.V. from the Le Ru *et al.* 2009 book.[39]

Another study by McMahon shed light on the impact of nonlocal effects on the Raman signal enhancement by utilizing FDTD.[41] It was found that nonlocal effects can decrease SERS enhancement by one order of magnitude in gold nanoparticles with a gap distance of 0.5 nm and produce blue-shifted plasmons.

Dimers & trimers *vs.* monomers: EF measurements in NP aggregates

Understanding of the nanogap effect can be explored in more detail with experimental methods involving the fabrication of the simplest agglomerated nanoparticles: dimers and trimers, as they represent the simplest nanostructure with nanogaps, which can be easily controlled. The most influential work on this topic was conducted by the group of Van Duyne.[20,47,48] They studied the structure of hot-spots for single-molecule SERS with dimers and their plasmonics with structure–activity relationships. According to their findings, the agglomeration of nanoparticles higher than that of dimers does not produce a significant increase in Raman signal enhancement. Also, experimental results and FDTD calculations showed that the highest enhancement factors (EF > 10^{10}) originate from nanogaps with gap distances lower than 1 nm. And even higher EFs can be achieved by a slight fusing of nanoparticles with the appearance of tiny crevices. These findings were made by observing 30 monomers, 6 dimers, and 12+ trimers of SiO_2 encapsulated AuNPs. A similar study, but with silver dimers, was done by Li *et al.*[49] They found that polarization-dependent EFs of dimers were found to be 1 to 10 higher than EFs for monomers, depending on polarization. Also, according to Steinigeweg *et al.*, the SERS intensity of the AuNP trimer is twice as large compared with the AuNP dimer.[50]

A simpler approach for the production and characterization of agglomerated nanoparticles was utilized by our group. We used mercapto carboxylic acid molecules as linkers for the fabrication of gold nanoparticle agglomerates.[51,52] We were able to produce and characterize 1224 SERS nanoantennae (533 dimers, 648 monomers, and 43 trimers) under conditions close to real-life applications. Also, by changing the carbon chain length of the mercaptan molecule, we were able to quantitatively assess the effect of gap distance change on the SERS signal. The characterization of each agglomerated nanoparticle was achieved by using a novel agglomerate characterization approach involving a combination of spectral and topographical maps. The results of the fabrication process and Raman measurement with a combination approach can be observed from TEM images and SERS intensity and EF plots in Fig. 3. By using the combination approach, we found that dimers produce up to 4.5 times higher signals than monomers. Also, we observed that dimerization of nanoparticles becomes more probable with a decrease in gap distance during the self-assembly process.

Importance of gap distance

The dependence of EM enhancement on the gap size was investigated extensively by both theoretical and experimental

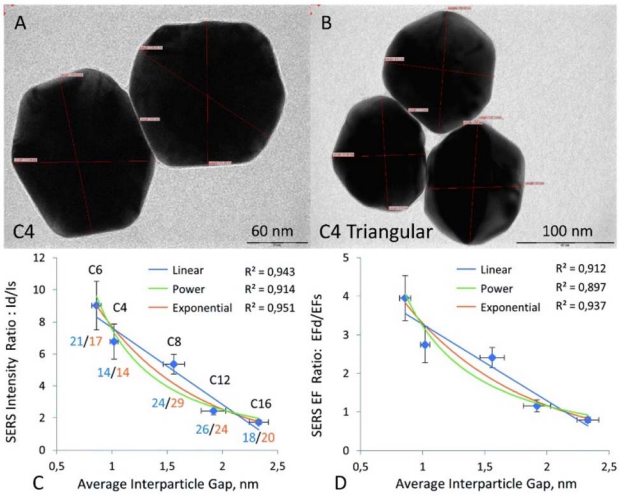

Fig. 3 (A and B) TEM images of the dimer and triangular trimer fabricated by self-assembly. (C) Plot of SERS intensity against the average interparticle distance. (D) Plot of the SERS EF ratio (EF dimer/EF single particle) *vs.* the average interparticle distance. The number of dimers/number of single particles is shown for each sample (blue, dimers; orange, single particles). Reproduced under Creative Commons License from an open-access Arbuz *et al.* 2022 article.[52]

methods. Electromagnetic considerations provide the following dependence of G_{SERS}^{EM} as a function of the distance (d) from the surface of a spherical nanoparticle of radius a.[8]

$$\frac{G_{SERS}^{EM}(d)}{G_{SERS}^{EM}(0)} = \left(\frac{a}{a+d}\right)^{12} \quad (8)$$

It is worth noticing that the distance dependence of the SERS signal is different from the enhancement dependence since the former also accounts for the number of illuminated molecules in shells at distance d from the surface, a number that scales as $(a + d)^2$.[8]

$$\frac{P_{SERS}(d)}{P_{SERS}(0)} = \left(\frac{a}{a+d}\right)^{10} \quad (9)$$

The above formulas suggest that the SERS enhancement and the signals drop very fast from the surface, and the analyte should normally be placed within 10 nm from the surface to efficiently exploit the plasmonic effect.

Several papers, including our own, investigated the distance dependence of SERS signal enhancement and control of gap distance. Most of these articles show the use of some sort of spacer as a tool to control the gap distance between plasmonic nanoparticles. For example, in Arbuz *et al.* publication, our group used mercapto carboxylic acids with different chain lengths and produced dimers with gap distances from 0.9 to 2.3 nm.[52] According to our data, we found that the dependence of gap distance on the Raman signal is more of an exponential form rather than the power of 10.[52] A different approach was used by Masango *et al.*; they deposited Al_2O_3 as a spacer by using atomic layer deposition (ALD) on top of an Ag film over

silica nanospheres (Ag-FON). This method helped them to achieve an angstrom level of precision in building gap distances from 0.1 to 3.3 nm.[53] An alternative spacer was proposed by Marotta *et al.* in the form of oligonucleotides, which were able to produce Ag nanorod aggregates with 1 to 6 nm gap distances.[54] Despite these examples of gap distance control, the problem of Raman signal reproducibility is still a major topic of concern, especially for single-molecule detection.

Reproducibility of SERS and structured substrates

Sensing and characterization of molecules are the main applications of SERS and other surface-enhanced techniques, in which the intensity of specific spectral peaks/bands is at the cornerstone. So, the reproducibility of signal enhancement is one of the most important parameters for surface-enhanced techniques and their biggest limitation for widespread use in routine applications. In addition, according to Natan and Lin *et al.*, uniformity and reproducibility are the main features of an ideal SERS substrate as well as high EF and stability.[55,56] And this issue is more profound for single-molecule detection applications, as the probability of finding a molecule in a hot spot with a sufficient level of EM field enhancement is very low.[37,38] One of the solutions for the reproducibility problem is to design and synthesize highly ordered nanostructures, which will produce sufficiently homogeneous nanogaps in size and morphology. In the last decade, research on this topic gained more attention with an increasing number of studies dedicated to the production of nanogaps by using nanofabrication techniques like atomic layer deposition,[58–64] electron beam lithography,[65–67] nanosphere lithography,[68–70] self-assembly,[71–74] and others. Moreover, nanostructures fabricated with these techniques were successfully used for single-molecule detection, with examples shown in Fig. 4.[57,75–78] Most of the nanogaps produced with these techniques can be classified into 5 different categories: interparticle nanogaps,[51,79–82] intraparticle nanogaps,[77,83–85] nanocrevice gaps,[86–88] nanogaps between nanoparticles and 2-D surfaces,[89,90] and nanogaps formed on the 2-D surface.[91–94] In this chapter, we will review fabrication techniques that produce these highly structured and reproducible nanogap substrates.

Electron beam lithography (EBL)

EBL is a nanofabrication technique with more than 4 years of development based on scanning electron microscopes developed in the early 1960s.[95] The process of EBL is illustrated in Fig. 5a.[96–98] In the first step, the layers of the conductive polymer and EBL resist are spin-coated on the surface of fused silica. Next, the desired pattern is drawn using a focused electron beam on an electron-sensitive polymer. The exposure to the electron beam modifies the solubility of the resist; in particular, positive resists become soluble after electron exposure and negative resists become insoluble after electron exposure. After that, the layer of the conductive polymer is removed, and the sample is developed by immersing it in a solvent that removes the soluble portion of the resist, generating the desired pattern. Etching or lift-off methods can now be used to create a metallic pattern. The metal can be deposited straight after the development stage, followed by removal of the polymer (lift-off), as shown in Fig. 5a, producing metal islands. In Fig. 5b, we can see gold nanodots with varying gap sizes prepared by using the EBL method with different exposure levels.[98] Alternatively, reactive ion etching (RIE) can be used to write the polymer pattern into

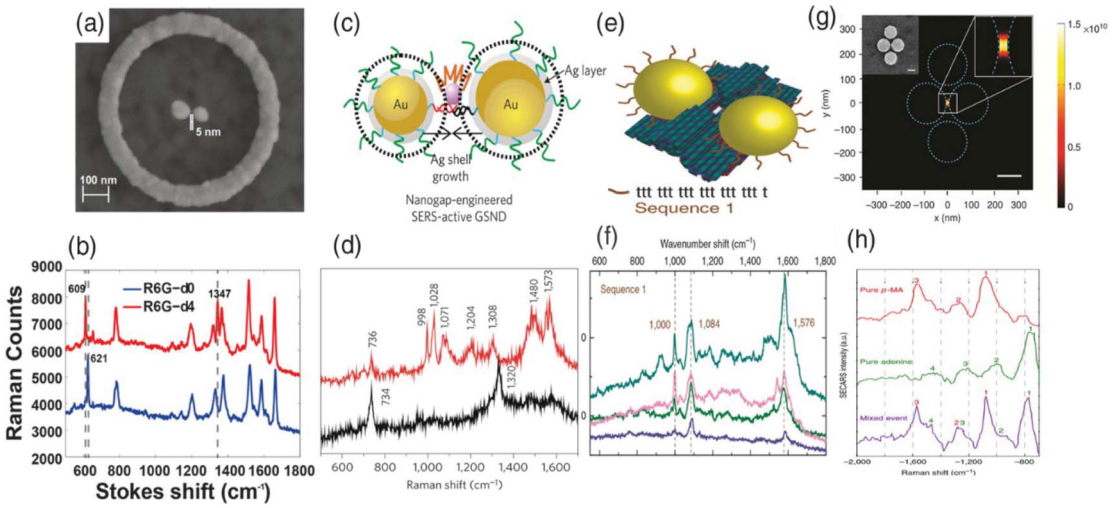

Fig. 4 Plasmonic nanogaps with precise size control for single-molecule SERS. (a) Scanning electron microscope image of an optical antenna. (b) Representative Raman spectra of R6G-d0 and R6G-d4 single-molecule level events. (c) Nanometer-scale silver-shell growth-based gap-engineering in the formation of the SERS-active GSND. (d) Raman spectra recorded from Cy3-modified oligonucleotides (redline) and Cy3-free oligonucleotides (blackline) in NaCl-aggregated silver colloids. (e) Schematic of the NP dimers assembled on the DNA origami platform. (f) Measured Raman spectra of the ssDNA coating of 19 bases of thymine (sequence 1) on the NP dimers. (g) SECARS enhancement map. (h) Three representative SECARS spectra showing a pure p-MA event (top), a pure adenine event (middle), and a mixed event (bottom). Reproduced under Creative Commons License from an open-access Yu *et al.* 2020 article.[57]

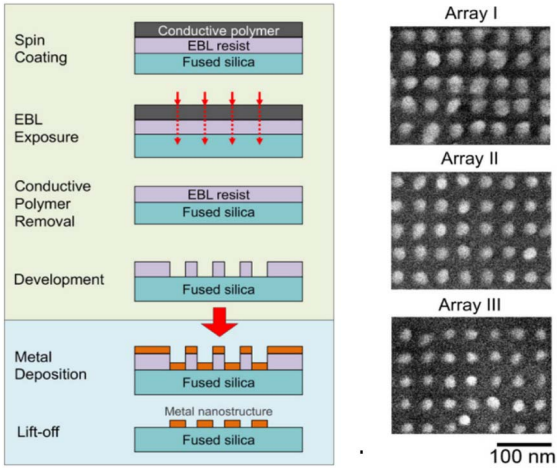

Fig. 5 Left side: scheme of electron beam lithography, metal deposition, and lift-off process steps employed to fabricate metallic nanostructures on dielectric substrates. Right side: SEM images of nanodot arrays prepared by EBL with different gap sizes. Reproduced with permission granted by the *Journal of Visualized Experiments* from the Peters *et al.* 2015 article.[98]

the substrate (the substrate is etched, but the polymer is not), then the polymer is removed and the metal is evaporated; in this case, the whole surface is covered with the metal.

EBL allows the geometry of the substrate to be finely controlled with a high degree of reproducibility; therefore, it is ideally suited for fabricating substrates whose properties have been theoretically engineered in order to optimize enhancement and to carry out structure–property studies. The best resolution is normally around 10–20 nm, which is significantly better than that obtained by standard optical lithography (limited by light diffraction).[100] For example, Zhu *et al.* fabricated sub-10 nm gaps by using a clever strategy.[99] In the first round of EBL fabrication and metal evaporation, an array of isolated multilayer gold/silver/chromium parallelepipeds was prepared. Afterward, chromium was oxidized to produce a controlled lateral swelling of the metal. The second round of EBL fabrication and metal evaporation was used to form nanoparticle dimers, whose gap was determined by the lateral expansion of the chromium. This process is illustrated in Fig. 6a, and a representative SEM image of the sample is presented in Fig. 6b. SERS measurements and simulations (Fig. 6c) demonstrated a two-order magnitude increase in the enhancement upon reduction of the gap, from 16 to 2 nm. Another example of the application of EBL in structured nanogap production was demonstrated by Ward *et al.*[101] They fabricated a "multibowtie" nanostructure by using EBL and electromigration. This structure consists of two larger pads with constrictions in between that have nanometer-scale gaps with sizes smaller than or equal to 5 nm. The FDTD calculation showed an approximate total EF of 5×10^8 by conservatively assuming the gap distance to be 2.5 nm. Likewise, Zhang *et al.* synthesized bowtie nanostructures to produce an array of nanogaps.[65] But they produced individual bowties with nanogaps, in contrast to the "multibowtie" structure by Ward *et al.* They were able to produce bowtie gap distances that varied from 24 nm down to 3 nm. This bowtie structure with a 6 nm gap was used to detect 1,2-di(4-pyridyl)ethylene (BPE) in different concentrations. The highest EF of 10^7 was achieved for the detection of 1 nM BPE. Different nanostructure geometries for nanogap formation were shown by Clark *et al.*[67] By using EBL, they fabricated silver multiple-split ring resonators with many nanometer-scale gaps smaller than 6 nm. This nanogap array was tested by using a DNA-hybridization assay. Results showed that these structures are capable of detecting approximately 50 DNA molecules per nanostructure and 10 DNA molecules per nanogap.

Overall, the electron beam lithography (EBL) method allows the preparation of highly ordered and uniform SERS substrates with nanostructures having a wide diversity of shapes and geometries compared with nanosphere lithography. However, the high cost of operation and the time-consuming procedure, in addition to forward scattering and backscattering problems, limit the use of this technique to produce large amounts of sensing platforms and subsequent commercialization.

Nanosphere lithography (NSL)

Another very effective fabrication method for the production of structured SERS substrates is nanosphere lithography, which was developed mainly by the efforts of the Van Duyne group and co-workers.[102,103] The technology is based on the assembly of polystyrene or silica spheres of suitable size on a clean substrate (glass, ITO glass, Si, or metal film), and by manipulating the assembly conditions, a monolayer or multilayer of the highly ordered nanosphere film will form on the substrate. The film is then utilized as a template for vacuum deposition or electrochemical deposition to generate a metal layer of the desired thickness on the template. As a result, three kinds of structured SERS substrates may be produced as illustrated in Fig. 7. The first one is a "film over nanosphere" (FON) substrate, synthesized by physical vapor deposition of a metal (*e.g.*, Ag or Au) on the nanosphere template. The second nanostructure is surface-confined nanoparticles with a triangular footprint made by the removal of nanospheres in the FON substrate by sonicating the entire sample in a solvent. Third is electrochemical deposition, followed by removal of the nanosphere, which leaves a thin nanostructured film containing a regular hexagonal array of uniform metal nanoislands, nanobowls, or nanovoids, depending on the thickness of the deposited film.[104,105] The advantage of using nanosphere lithography to prepare the SERS substrate is that the shape, size, and spacing of the nanostructures can be controlled by the size of the nanospheres and the thickness of the deposited metal, allowing the LSPR position to be adjusted to match the excitation wavelength and achieve optimized SERS enhancement.[106] Methods 1 and 3 will result in substrates with significant SERS enhancement. Even though the SERS activity of the second technique is rather low due to the considerable spacing between particles, the excellent LSPR tenability results in an excellent LSPR sensing chip. Although obtaining an ordered substrate with an area of 10–100

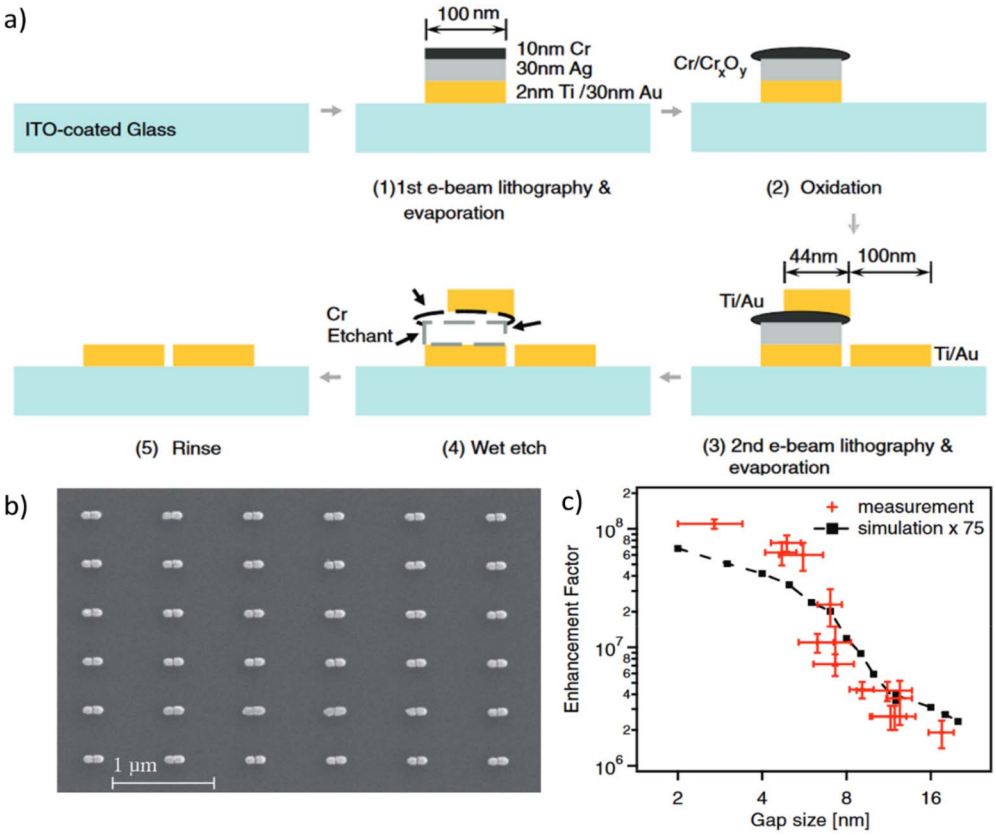

Fig. 6 (a) Fabrication process for sub-10 nm gaps; (b) SEM image of the fabricated array of dimers; (c) experimental and theoretical SERS enhancement as a function of the gap. Reproduced with permission granted by John Wiley & Sons from the Zhu *et al.* 2011 article.[99]

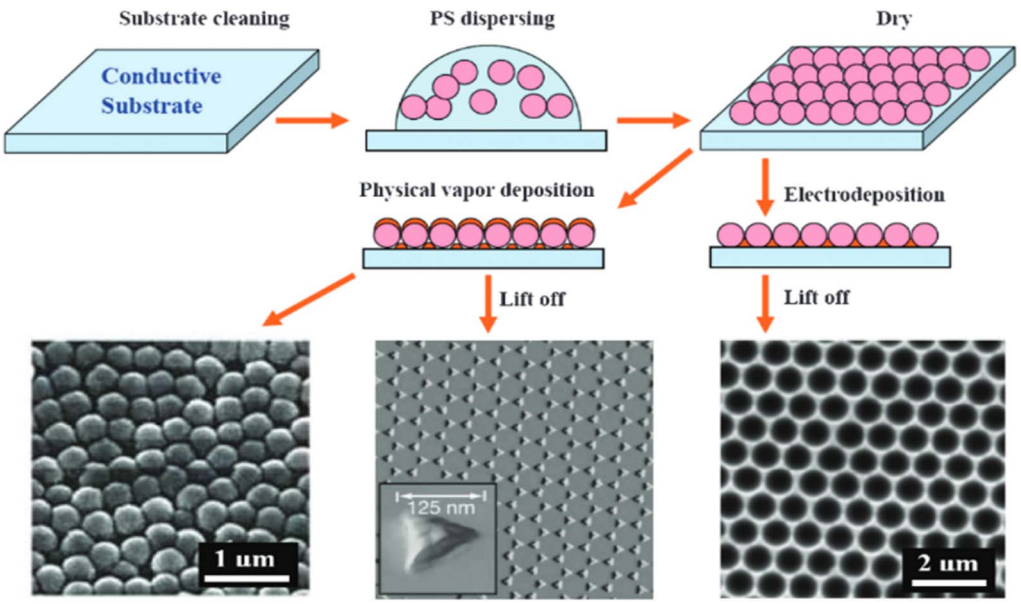

Fig. 7 Schematic diagram of template methods using nanosphere lithography to fabricate ordered nanostructured SERS-active substrates. Reproduced with permission granted by the Royal Society of Chemistry from the Wu *et al.* 2008 article.[104]

m^2 is rather common in some experienced groups, the success rate of this procedure is dependent on the experimentalist's experience and how rigorously the experimental conditions can be regulated.[107] When the size of the sphere is less than 200 nm, obtaining an ordered surface with no point or line flaws is extremely difficult. However, with the aid of a microscope, it is

still possible to locate an ordered area for quantitative analysis that has high reproducibility and stability.

The advantages of this method in the formation of long-range ordered nanostructure arrays spurred numerous research studies and subsequent possible applications. One such application was demonstrated by Wang *et al.*, where they prepared an Au/Ag bimetallic nanostructure array by NSL.[68] They were able to fabricate "V" and "Y" shaped nanogaps with a gap distance as low as 3 nm by depositing an Au/Ag film on 200 nm polystyrene spheres. And by using a 4-mercaptopyridine (4-Mpy) analyte, they calculated the EF of this nanostructure, which is 1.66×10^9. A similar level of signal enhancement was presented by Sawai *et al.*[69] They used angle-resolved NSL (AR-NSL), developed by a group led by Van Duyne, to produce an array of Ag dimers with a gap distance of approximately 10 nm.[108] The Raman measurement of 4,4′-bipyridine molecules with this nanostructure showed a strong peak at 1018 cm^{-1} (ring breathing), which translates to an enhancement factor in the range of 10^5–10^9 with an even higher EF if it was calculated in hot spots. In addition to these techniques, the combination of NSL with atomic-layer deposition (ALD) is becoming a popular variation for the production of 3D nanogap arrays. One of such studies is presented by Im *et al.*, where they produced hybrid Ag/air/Ag nanorings by using an Ag-FON substrate modified with an Al_2O_3 layer by ALD (Fig. 8).[70] The final nanostructure had well-defined 10 nm nanogaps around each nanosphere and showed an EF of 10^8 and a LOD for adenine of 76 pM, which are significantly better than the results of similar experiments for plain Ag-FON substrates.

A different approach for the combination of ALD with NSL was shown by Li *et al.* by producing a particle-in-bowl nanostructure, which consists of an Ag nanoparticle in an Au bowl.[64] They were able to obtain a spatially averaged SERS EF of 3.8×10^7 for the rhodamine 6G molecule with nanogap sizes of 5–15 nm. By using a similar approach, the Cai *et al.* group produced annular nanogap arrays with 1–10 nm gap distance and even sub-1 nm gap separation.[60] They produced a nanostructure which was then used to quantitatively detect the 4-ATP molecule in the concentration range of 1 pM–10 nM and resulted in an LOD of 10 pM and EF of 3.1×10^6. With this method, they were able to produce a densely packed array of ultrasmall and uniform nanogaps, which can be used in numerous nanophotonic and nanoelectronics applications.

To sum up, the NSL method is more straightforward, cost-effective, and material agnostic than conventional lithography methods like EBL to produce highly ordered nanogap

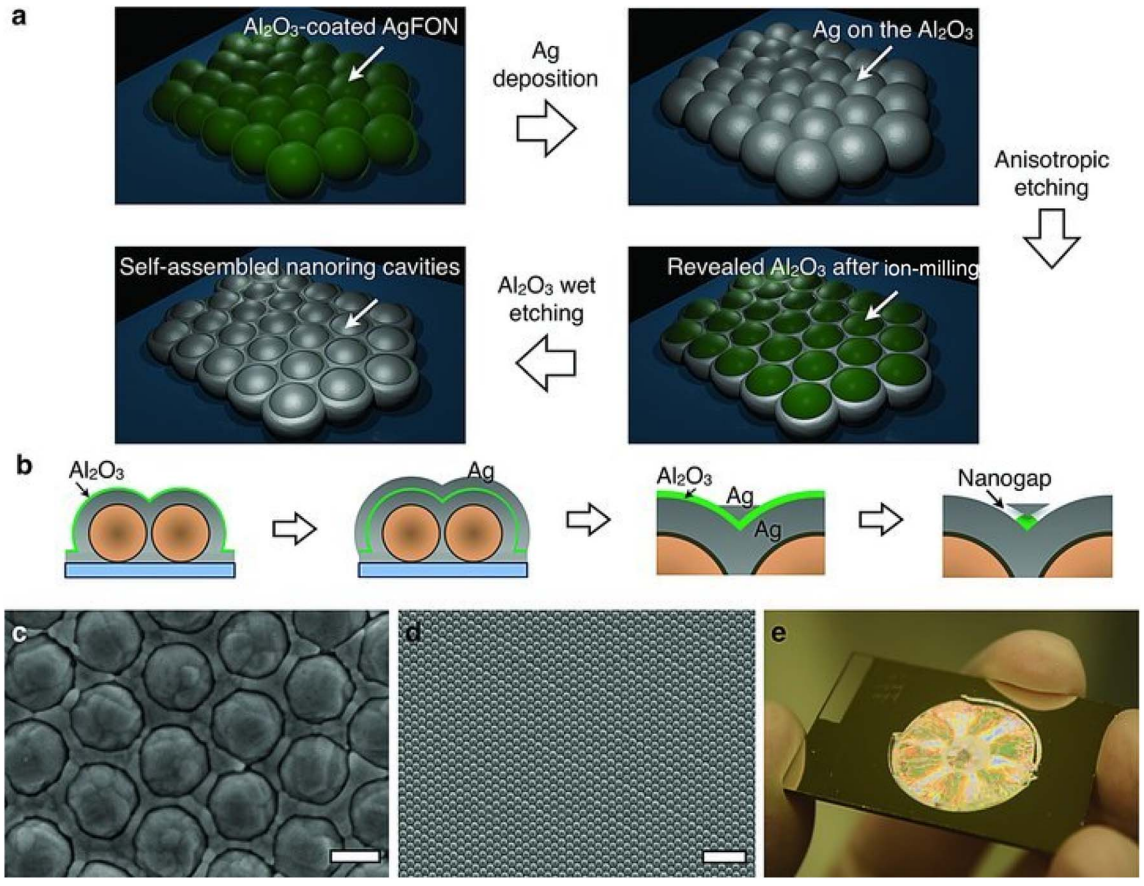

Fig. 8 (a) A schematic of the fabrication process for plasmonic nanoring cavities using nanosphere lithography and atomic layer deposition (ALD). (b) Cross-sectional schematics of the fabrication process. (c) Scanning electron micrograph (SEM) of the nanoring cavities on the FON substrates. Scale bar: 200 nm. (d) SEM image of the nanoring cavity array formed over a 16 μm × 10 μm area. (e) Photograph of the nanoring cavity (FON-gap) sample. Reproduced with permission granted by John Wiley & Sons from the Im *et al.* 2013 article.[70]

arrays.[105,109] However, there are still some challenges associated with this method concerning stability and morphology. For example, plasma and heat treatments required to alter the size of the nanospheres in most cases produce problems in morphology, like rough surfaces, irregular shapes, and non-uniform sizes.[110,111] Consequently, the non-uniformity in the morphology of nanospheres affects the performance of the resulting nanostructure, which is even more problematic when the size of the nanosphere is reduced below 50%.[112] Nevertheless, further research on different approaches for nanosphere etching will help reduce the issues in morphology.

Template-assisted (TA) fabrication

Template-assisted electrochemical deposition (TAED) allows the deposition of metals with controlled geometry and disposition by using inorganic ordered templates, such as silica[113] and alumina,[114] or a polymeric template polycarbonate.[115] Polymeric membranes or microspheres, as well as custom alumina membranes, are commercially available. In addition, anodization of aluminum foil or a thin aluminum film produced by sputtering over a conducting substance can be used to make alumina templates. Self-organization leads anodization to generate channel arrays with a high aspect ratio and regular pore layouts.[116] In the case of silica, the template is formed by applying a suitable cathodic potential to an electrode immersed in a surfactant-containing hydrolyzed solution, which produces the hydroxyl ions required to catalyze polycondensation of the precursors and self-assembly of hexagonally packed one-dimensional channels that grow perpendicular to the electrode surface. Following template construction, metal deposition is performed under galvanostatic conditions using either constant or alternating current deposition, and the template is then removed, leaving free-standing metal nanostructures. The fabrication process of an array of nanorods is summarized in Fig. 9.[116] This methodology can produce large arrays of nanogaps with a controlled size between 5 and 25 nm, which can be observed in Fig. 9g and h. Numerous research studies were conducted on this fabrication method to prepare SERS substrates with good enhancements.

One such study was done by Tian *et al.*, in which they used a mesoporous silica template in combination with nanocasting to produce a plasmonic Ag superstructure.[87,117] The resulting nanostructure can be seen in Fig. 10. The gap distances in this nanostructure were approximately 2 nm in size and highly uniform. The signal enhancement properties of this nanogap array were measured by using crystal violet (CV) dye and showed an EF of 10^9 and LOD of 0.1 fM. An earlier example of template-mediated nanogap array formation was presented by Baik *et al.*, where they used an anodic alumina template to produce silver nanowires with gap distances ranging from 17 nm to 40 nm.[118] A similar methodology with a different nanostructure was presented by Hao *et al.*[90] They fabricated a highly ordered and uniform array of dimers by using anodic aluminum oxide as a template and angle-resolved shadow deposition. The gap distance between dimers varied from 8 to 18 nm by changing the angle of shadow deposition. Also, by changing the deposition rate, they were able to produce heterodimers of different sizes. FDTD calculations for this substrate showed a theoretical EF of 1.4×10^8. Even lower gap distances and a subsequently higher EF were achieved by Fu *et al.* with their ultrathin alumina mask (UTAM) surface pattern technique.[119]

Overall, template-assisted deposition is an efficient method for the production of ordered and uniform nanogap arrays. However, the morphology and gap distance are highly dependent on template fabrication, like in the case of NSL, which can

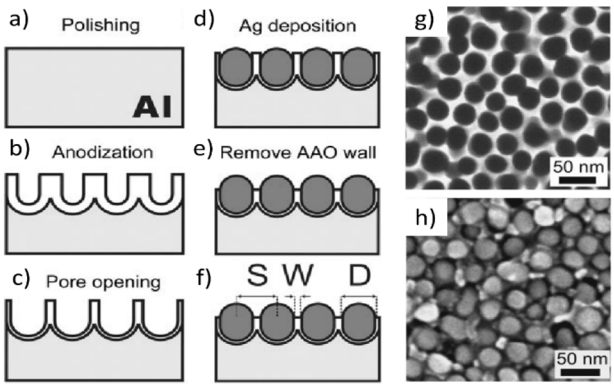

Fig. 9 Steps involved in the fabrication of a hexagonal array of metallic nanopillars with the anodic alumina template method. (a) Aluminum foil is polished; (b) an array of vertically aligned nanopores is produced by anodization; (c) pores can be widened by etching with a phosphoric acid solution to tune the wall thickness and hence the gap size in the final structure; (d) silver is electrodeposited in the pores forming nanopillars of controlled height; (e) alumina is partially etched to expose the silver nanopillars; (f) the final array is characterized by interparticle distance S, interparticle gap W and nanopillar diameter *D*; (g) and (h) SEM images of the AAO substrate before and after Ag deposition. Reproduced with permission granted by John Wiley & Sons from the Wang *et al.* 2006 article.[116]

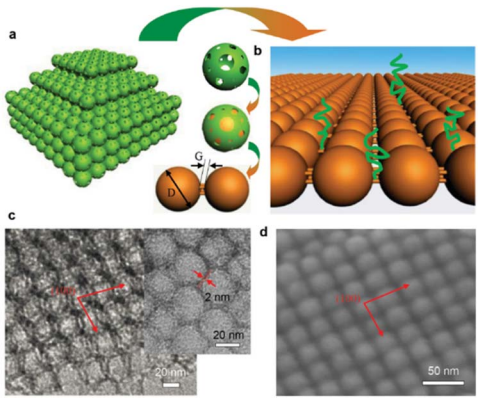

Fig. 10 The ordered mesoporous template strategy to synthesize silver plasmonic supercrystals. (a and b) Schematic diagram of the synthesis procedure for ordered silver supercrystals by means of a nanocasting process using different templates with a variety of pore sizes and wall thicknesses, (c) TEM image of the template OMS-28, (d) SEM image of OMASC-28. Reproduced with permission granted by John Wiley & Sons from the Tian *et al.* 2015 article.[87]

Table 1 SERS studies involving nanogaps[a,b]

Year, author	Nanostructure	Preparation	Gap width (nm)	Analyte	LOD (M)	EF
2011, Lim *et al.*[125]	Gold nanobridged nanogap particles (Au-NNP)	DNA-based synthesis	1	Cy3	1.00×10^{-14}	1.00×10^{8}
2011, Liu *et al.*[91]	Au nanoporous film (NPFs)	Capping agent replacement induced self-organization of ultrathin nanowire (CARISUN) strategy	1.5	BPE	1.00×10^{-10}	1.00×10^{9}
2012, Oh *et al.*[126]	Glass nanopillar arrays with nanogap-rich silver nanoislands	Reactive ion etching (RIE) of glass with an annealed silver nanoisland mask and an additive silver deposition	10	DNA bases	1.00×10^{-8}	5.30×10^{7}
2012, Wu *et al.*[127] (*)	Au-coated plasmonic nanodome array (PNA)	Low-cost, large-area nanoreplica molding processes	10	Urea	1.19×10^{-2}	8.51×10^{7}
2013, Chen *et al.*[92]	Ag SERS-active substrate	High-pressure sputtering technique	10	R6G	2.00×10^{-9}	3.48×10^{5}
2013, Im *et al.*[70]	AgFON substrates with ultrathin gaps	NSL with ALD	10	Adenine	7.60×10^{-8}	1.00×10^{8}
2014, Shao *et al.*[86]	Ag nanoislands and Ag nanoflowers on chitin nanopillar arrays	One-step and reagent-free top-view dc ion-sputtering techniques	10	R6G	1.00×10^{-13}	5.80×10^{7}
2014, Lee *et al.*[128]	Au–Ag head–body nanosnowmen	DNA-modified AuNPs (DNA-AuNPs) as seeds and adding Ag precursors	1	Cy-5 dye	5.00×10^{-15}	1.00×10^{8}
2014, Zhao *et al.*[83]	Core–shell gold nanostructures	polyA-mediated interior nanogaps encoded by non-fuorescent small molecules	1	HAV; HBV; HIV target DNAs	3.90×10^{-13}; 1.80×10^{-13}; 5.10×10^{-13}	1.33×10^{8}; 1.33×10^{8}; 1.33×10^{8}
2014, Cheng *et al.*[89]	Ag nanocubes on the massed Ag mirror	Thermal evaporation	1.75	R6G	1.00×10^{-9}	2.80×10^{8}
2014, Song *et al.*[85]	Au core–shell NPs	Nanoparticle-templated self-assembly	2	MCF-7 cells	30 cells per ml	1.40×10^{8}
2015, Shen *et al.*[129]	Gold–silver nano-mushrooms	DNA-mediated approach	1.5	ROX	NA	1.20×10^{9}
2015, Hakonen *et al.*[80]	AuNP dimer on a mirror	Hole-mask colloidal lithography	7.1	*trans*-1,2-bis(4-pyridyl)ethylene (BPE)	2.70×10^{-14}	2.1×10^{11}
2015, Zhang *et al.*[65]	Au bowties	EBL	6	BPE	1.00×10^{-8}	1.00×10^{7}
2015, Tabatabaei *et al.*[130]	3D plasmonic cavity nanosensor	EBL	3	4-Nitrothiophenol (4-NTP)	1.00×10^{-16}	1.00×10^{7}
2015, Tian *et al.*[87]	Ag plasmonic supercrystals	Template assisted nano-casting	2	CV	1.00×10^{-16}	1.00×10^{9}
2015, Tian *et al.*[117]	Ordered mesoporous Ag superstructure	Template assisted nano-casting	2	CV	1.00×10^{-13}	1.00×10^{9}
2015, Fu *et al.*[119]	Ag NP arrays	Ultrathin alumina mask (UTAM) surface pattern technique	5	R6G	1.00×10^{-10}	1.00×10^{9}

Table 1 (*Contd.*)

Year, author	Nanostructure	Preparation	Gap width (nm)	Analyte	LOD (M)	EF
2016, Jeong *et al.*[131]	Vertically stacked 3D crosspoint plasmonic nanostructures	Solvent assisted nanotransfer printing (SnTP)	5	R6G	1.00×10^{-11}	4.10×10^{7}
2016, Li *et al.*[132]	Au@AgAuNPs	Etching	1	PSA; CRP	1.92×10^{-11}; 7.70×10^{-12}	1.00×10^{6}; 1.00×10^{6}
2017, Pham *et al.*[133]	SiO_2@Au@Ag NPs	Au seed mediated Ag growth method	4.2	4-ATP	2.40×10^{-9}	4.20×10^{6}
2017, Li *et al.*[73]	P(AAm-*co*-AA) hydrogel microsphere @ Au nanosphere	Self-assembly based on electrostatic interaction	6	4-ATP	1.00×10^{-11}	1.00×10^{9}
2017, Cao *et al.*[62]	Au nanoparticles (NPs)/ nanogap/Au NPs	Rapid thermal annealing (RTA), atomic layer deposition (ALD) and chemical etching processes	2	MB	1.00×10^{-10}	1.00×10^{7}
2017, Sergiienko *et al.*[51]	AuNPs and AgNP agglomerates	Self-assembly	10.6	2-MOTP	1.00×10^{-9}	1.00×10^{10}
2017, Eom *et al.*[88]	Au nanowires	Deposition of nano-particles on single-crystalline Au NWs	10	HeLa cancer cells	0.2 cell per ml	1.34×10^{4}
2018, Jin *et al.*[71]	AuNP array	Block copolymer self-assembly	9	Adenine	1.00×10^{-7}	1.00×10^{4}
2018, Zhang *et al.*[134] (*)	Ag nanoflowers on a graphene@Cu net (AgNFs/G@Cu)	Electro-deposition and vapor phase deposition	20	R6G; CV	1.00×10^{-14}; 1.00×10^{-12}	2.74×10^{10}; 7.21×10^{9}
2018, Kim *et al.*[84]	Dealloyed intra-nanogap particles (DIPs), Au/Au–Ag core/alloy shell nanoparticles	Selective-interdiffusive dealloying chemistry	2	DNA probe	1.00×10^{-17}	1.10×10^{8}
2018, Yang *et al.*[135]	Perpendicular sandwich-like Au@Al_2O_3@Au hybrid nano-sheets (PSHNs)	Solvothermal synthesis and a follow-up Au NP graft	1.7	Rhodamine B	1.00×10^{-18}	1.00×10^{12}
2018, Pan *et al.*[136]	Three-dimensional (3D) sub-10 nm Ag/SiNx gap arrays	Stress-induced nanocracking of a SiNx nanobridge and Ag nanofilm deposition	10	R6G	1.00×10^{-16}	1.00×10^{8}
2018, Cai *et al.*[60]	Ultranarrow annular nanogap arrays (ANAs)	NSL with ALD	5	4-ATP	1.00×10^{-11}	3.10×10^{6}
2018, Wu *et al.*[137]	Periodic AuNP array bilayer	EBL	10	R6G	1.00×10^{-13}	2.2×10^{7}
2019, Kwak *et al.*[138]	Nanogap-rich Au nanoislands on the top surface of a single multimode fiber	Repeated solid-state dewetting of thin Au films	10	CV	1.00×10^{-7}	7.80×10^{6}
2019, Yang *et al.*[139]	Ag nanogap shells (AgNGSs) on SiNPs	Modulation of chemical reaction kinetics	2	AD biomarkers	5.54×10^{-14}	1.10×10^{7}
2019, Guo *et al.*[140]	AuNPs	Micro-nanomachining technology	1	CV; R6G	1.00×10^{-20}; 1.00×10^{-20}	NA; NA
2020, Lao *et al.*[141]	Au film	Supercritical drying-switchable capillary-force self-assembly (CFSA)	2	Anticancer drugs (DOX)	1.00×10^{-4}	8.00×10^{7}

Table 1 (*Contd.*)

Year, author	Nanostructure	Preparation	Gap width (nm)	Analyte	LOD (M)	EF
2021, Adhikari *et al.*[142]	AuNPs	Template assisted fabrication using SiO_2 nanopillasr	10	TNT; RDX; PETN	1.00×10^{-12}; 1.00×10^{-11}; 1.00×10^{-11}	NA; NA; NA
2021, Shafi *et al.*[143]	Ag NPs/HMM	Comprising a monolayer of Ag NPs and Au–Al_2O_3 films	10	Rhodamine 6G	1.00×10^{-12}	1.72×10^{8}
2022, Zhao *et al.*[144]	AuNPs	Combination of photolithographic metal patterning, swelling-induced nanocracking, and superimposition metal sputtering	10	Rhodamine 6G	1.00×10^{-4}	1.00×10^{6}
2022, Zhao *et al.*[144]	AgNPs	Combination of photolithographic metal patterning, swelling-induced nanocracking, and superimposition metal sputtering	8	Rhodamine 6G	1.00×10^{-14}	1.10×10^{7}
2022, Bock *et al.*[145]	SiO_2@Au@Au NPs	Template assisted fabrication	1	4-Fuorobenzenethiol	1.20×10^{-4} (16 μg ml^{-1})	3.83×10^{6}
2023, Teng *et al.*[146]	CB[8]-linked AuNPs	Frens method synthesis and mixing with CB[8]	1	Estrone; bisphenol A; hexestrol	3.75×10^{-6}; 1.19×10^{-6}; 8.26×10^{-6}	5.00×10^{4}; 2.50×10^{5}; 2.00×10^{5}
2024, Adhikari *et al.*[147]	Gold hole-sphere nanogap	EBL	7	Adenine; guanine; cytosine; thymine	1.00×10^{-11}; 1.00×10^{-10}; 1.00×10^{-10}; 1.00×10^{-8}	4.60×10^{8}; 4.60×10^{8}; 4.60×10^{8}; 4.60×10^{8}
2024, Lee *et al.*[148]	Annular Au nanotrenches	Seed-mediated growth; selective deposition and etching-based growth	1	SARS-CoV-2 spike glycoprotein	1 fg ml	1.1×10^{9}
2024, Sibug-Torres *et al.*[149]	Multilayer aggregates of AuNPs/cucurbit[5]uril (MLagg-CB[5])	Self-assembly of 80 nm Au nanoparticles with cucurbit[5] uril (CB[5]) scaffolds on an FTO substrate	0.9	Adenine	1.00×10^{-7}	1.00×10^{6}
2024, Zhao *et al.*[150]	Open-gap Au/AgAu monolayer	Hydrothermal method, chemical etching, and interfacial self-assembly	8	CV	1.00×10^{-10}	2.20×10^{8}
2025, Lv *et al.*[151]	Au/covalent organic frameworks (Au/COFs)	Seed-mediated growth with citrate reduction, hydroxylamine-assisted growth, and COF encapsulation	3	Rhodamine B; methylene blue; CV	7.20×10^{-10}; 7.82×10^{-10}; 8.44×10^{-11}	1.34×10^{8}
2025, Suster *et al.*[152]	Core–shell-like nanostructures (CSLNs)	Deposition of negatively charged DNSs; physical vapor deposition of a germanium wetting layer and a plasmonic metal	8.5	*p*-mercaptobenzoic acid	3.70×10^{-7}	1.00×10^{6}
2025, Li *et al.*[153] (*)	AuAg@gap@AuAg NS	One-pot preparation, PEI-guided Ag-deposition, galvanic replacement reaction and co-reduction	14.5	Hg(II)	3.30×10^{-13}	2.00×10^{8}

Table 1 (*Contd.*)

Year, author	Nanostructure	Preparation	Gap width (nm)	Analyte	LOD (M)	EF
2025, Wu *et al.*[154] (*)	Wafer-scale plasmonic metamaterial sheet (PLAMS)	Spin-coating, plasma treatment, RIE, e-beam evaporation metal deposition, and ICP-CVD	≥1	*trans*-1,2-bis (4-pyridyl)-ethylene	NA	1.17×10^6
Average gap (nm)	Median gap (nm)	Average LOD (M)		Median LOD (M)	Average EF	Median EF
3.89	5.0	1.17×10^{-11}		1.00×10^{-11}	6.00×10^7	1.00×10^8
Average gap (nm)	Median gap (nm)	Average LOD (M)		Median LOD (M)	Average EF	Median EF
3.52	5.0	1.01×10^{-11}		1.00×10^{-11}	5.06×10^7	1.00×10^8

[a] We also decided to do the same statistical calculations excluding the papers where the gap is > 11 nm (ref. 134) and LOD is $>10^{-3}$ M (excluded articles are noted with an asterisk sign). [b] NA not available.

produce serious problems during the deposition stage. Thus, novel template production methodologies need to be implemented for this technique to improve and obtain new applications in surface-enhanced spectroscopies.

Unstructured SERS enhancement

Despite the presence of numerous techniques that can produce highly structured arrays of nanostructures with nanometer-level nanogaps, their cost, speed, and complexity make the scalability for future commercial use very problematic. On the other hand, techniques involving unstructured fabrication of nanogaps are easier to perform, less expensive, and readily scalable. Also, such platforms exhibit quite significant levels of SERS signal enhancement and can be used for quantitative research. These methodologies are based on the aggregation of nanoparticles in solution.[120]

The majority of nanoparticles utilized for SERS investigations in solutions are spherical silver and gold colloids. They are frequently made by reducing a precursor salt in water with sodium citrate; the citrate deposited on the surface of the nanoparticles also serves as an electrostatic stabilizer.[121,122] For silver and gold, the localized surface plasmon resonance typically peaks at around 400 and 520 nm, respectively. Spherical nanoparticles can also be fabricated by laser ablation.[123,124] In this scenario, a metal target is placed at the bottom of a solution and a pulsed laser is closely focused on its surface; the heating and photoionization processes lead the metal to change the aggregation state, generating liquid drops, vapors, or a plasma plume. The target's atomized material condenses, resulting in the production of nanoparticles.[123,124] Nanoparticles can be created *via* laser ablation from a variety of materials, with or without capping agents, by selecting the right target plate. The absence of capping agents facilitates the functionalization of nanoparticles (Table 1).

The simplest process for inducing nanoparticle aggregation is to increase the ionic strength of the colloid by adding an electrolyte, which reduces the coulombic repulsions that ensure nanoparticle stability. Different groups of aggregating agents can be distinguished based on the degrees of alteration induced into the colloidal system.[39] For example, passive electrolytes, such as KNO_3 and $MgSO_4$, merely increase the ionic concentration without firmly binding the metal surface, whereas active electrolytes (such as the halide salts NaCl and KBr) significantly modify the nanoparticle surface chemistry *via* strong halide–metal interactions, particularly in the case of Ag.[155,156] Randomly aggregated large nanoparticle ensembles have been found to produce significant SERS amplification, allowing SERS to identify single molecules.[18,19] Uncontrolled nanoparticle assemblies, even from highly monodisperse systems, have poor consistency in terms of interparticle spacing, shape, and particle counts per cluster. One of the ways that this issue can be solved is by employing molecular nanoparticle cross-linkers to self-assemble nanoparticle aggregates and engineer nanogaps in a controllable manner.

Self-assembly mediated by molecular linkers

The use of molecules as nanoparticle cross-linkers has been shown to be a more efficient strategy to control and design

interparticle properties and the geometrical structure of Ag and Au clusters. It is possible to generally classify molecular linkers into two major categories: non-biological linkers and biological linkers. Also, these molecular linkers can be classified based on their mode of work: bifunctional molecules and molecules with selective recognition ability. The difference between these types stems from the mode of link; in the latter type, the assembly is triggered by some external factor like a change in pH or UV irradiation, whereas the former bonds nanoparticles constantly through covalent bonds or electrostatic interactions.[120]

Non-biological linkers

Extensive research on the use of bifunctional molecules to engineer hot-spots into SERS active nanostructures was pioneered by Moskovits and co-workers, who successfully employed various classes of linkers such as dithiol- and diamine-containing molecules.[157–159] Vlckova *et al.*, for example, explored single-molecule SERS at individual hotspots of silver dimers generated by small cluster assembly utilizing 4,4′-diaminoazobenzene as a bifunctional linker with a high Raman cross-section.[160] A linker-to-nanoparticle ratio of about 1 to 1 was used to limit the dispersion of aggregates to very small ones dominated by dimers and to statistically pinpoint a single bifunctional molecule at the hot spot. SERS spectra recorded on a single dimer level after chemical deposition on TEM finder grids revealed temporal fluctuations (blinking) with large repetition durations, which were most likely caused by single-molecule dynamics.

Bifunctional compounds with nanoparticle-bridging ability and high Raman cross-sections are especially well suited for the creation of SERS-encoded clusters for extrinsic applications. For example, Fabris and colleagues reported high-yield production of Ag dimers in suspensions *via* controlled aggregation utilizing distyrylbenzene or 4,4′-dimercaptobiphenyl.[161] Following that, 4,4′-dimercaptobiphenyl-linked Ag dimers were functionalized with aptamer sequences to impart selective recognition properties and their application as an effective SERS-encoded substrate for protein detection. A different approach for the non-biological linkage was demonstrated by Cong *et al.*, where they produced an array of AuNPs with biocompatible silicon nanotubes as an external linker.[74] The linking of nanoparticles with the help of silicon nanotubes was probably an effect of solvent evaporation-assisted capillary forces. With this methodology, they produced sub-1 nm nanogaps with an EF of 3.1×10^7 and with application in *in vivo* pH measurement. Intraparticle nanogap fabrication with a non-biological linker was demonstrated by Song *et al.*[85] They were able to produce sub-10 nm intraparticle gaps by self-assembly of amphiphilic block copolymers around an Au nanoparticle with subsequent formation of an Au nanoshell around it. The EF calculation showed a signal enhancement of 1.4×10^8 order and detection of MCF-7 by MUC-1 aptamers yielded a 30 cells per ml limit of detection.

Biological linkers

Biomolecules, including antibodies and antigens, proteins, and DNA, have also been used to successfully build metallic nanoparticles. Because of its extraordinary properties, such as molecular recognition, structural plasticity, and programming

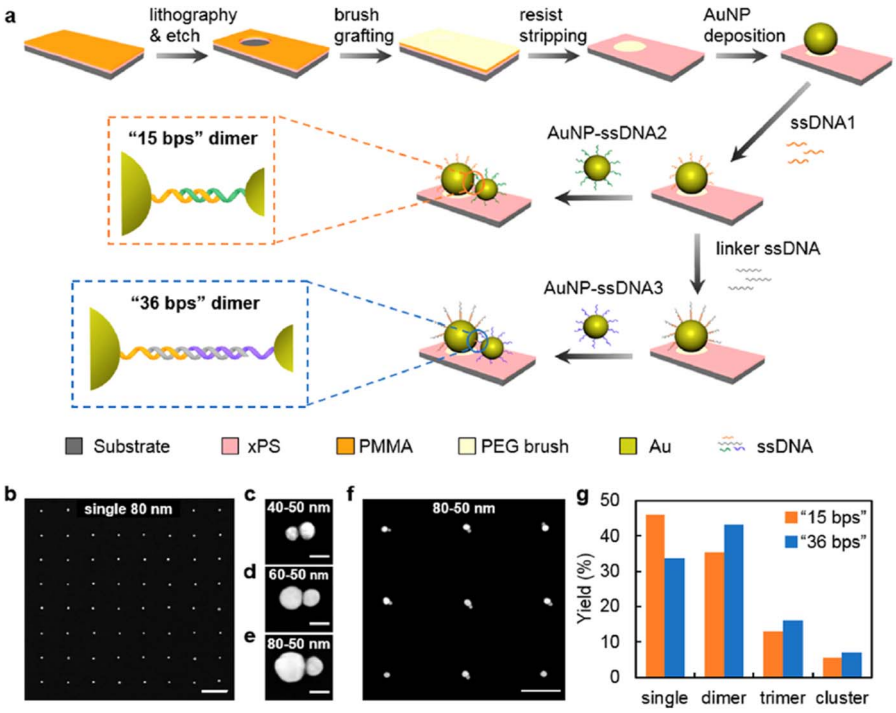

Fig. 11 Fabrication of AuNP heterodimer arrays. (a) Schematic of the hierarchical assembly of AuNP heterodimers. (b) The yield of single-AuNP arrays is essentially 100%. Single-AuNP arrays are then functionalized with ssDNA1. (c)–(e) Heterodimers of 40–50, 60–50, and 80–50 nm sizes can be readily assembled following the hierarchical approach. (g) Dominant structures after assembly are heterodimers and single AuNPs. Reproduced with permission granted by the American Chemical Society from the Li *et al.* 2019 article.[82]

capabilities to precisely direct nanoparticle organization into an impressive variety of complex morphologies, including post-assembly reconfiguration of plasmonic nanostructures *via* molecular stimuli, DNA is one of the most outstanding materials for bottom-up engineering of rationally designed plasmonic nanoparticle assembly.[162–164]

Graham and colleagues pioneered reversible aggregation of oligonucleotide-functionalized nanoparticles incorporating a Raman reporter *via* ssDNA hybridization to alter SERS signals, which was followed by Nie and colleagues.[165,166] Silver and gold nanoparticles were functionalized with DNA probes and tagged with dye molecules as Raman reporters in these investigations. The addition of a target sequence that is complementary to the two probe sequences results in sequence-specific DNA hybridization, which dictates extended nanoparticle aggregation and, as a result, an increase in the SERS signal. Subsequent heating of the colloidal system promotes cluster disassembly *via* DNA duplex denaturation, resulting in the removal of the extra SERS enhancement due to interparticle connection creation. Built on these studies, the recent work of Li *et al.* explores the fabrication of heterodimers with nanogap distances of sub-5 nm.[82] The process of DNA-mediated heterodimer synthesis and its results can be observed in Fig. 11. The Raman measurement of the Cy5 dye resulted in an EF of the 10^5–10^6 order. Despite a lower EF than that of other nanostructures, this type of nanogap is less susceptible to small changes in interparticle separations as compared to much narrower gaps, providing SERS substrates with quantitatively predictable enhancements.

As for other biological linkers, Wang *et al.* created an asymmetric assembly of spherical gold nanoparticles and gold nanorods, respectively, functionalized with a thrombin-binding aptamer and an anti-thrombin antibody for the detection of thrombin in human blood serum at subnanomolar levels.[167] Linkage through antibodies and antigens is also possible, which is shown by numerous studies on sandwich SERS immunoassays, including several from our group.[168] In these studies, we studied the use of a Si wafer substrate with gold nanoparticles for the quantitative assay of the human immunoglobulin antibody biomarker, which also serves as a linker between the nanoparticles and gold substrate surface nanoparticles.

Comparison with other fabrication methods

Despite clear advantages of the self-assembly process over ordered fabrication methods (lithography and template-assisted deposition) in terms of low-cost, simplicity, and scalability, a more quantitative approach for comparison of these methods in terms of figures of merit would be useful. To make such a comparison, we compiled references for each major nanogap fabrication technique and assessed them in terms of attainable gap distance and enhancement factor. A compact representation of the results for this endeavor can be observed in Table 2. From this table, we can observe that the average gap distances are the lowest for the self-assembly and template-assisted techniques (2.34 and 3.74 nm), followed by EBL (5.28

Table 2 Comparison of fabrication techniques[a]

Fabrication method (38 papers; EF and LOD)	EF			LOD, M			Average gap distance and range, nm	Average RSD	Price	References
	Average	Median	Range	Average	Median	Range				
EBL (6 and 4)	1.2×10^8	4.6×10^8	1.0×10^7–5.0×10^8	1.4×10^{-11}	1.0×10^{-10}	1.66×10^{-17}–1.00×10^{-8}	5.28 (2.5–10)	N/D	$$$	65, 99, 101, 130, 137 and 147
NSL (7 and 4)	7.92×10^7	1.00×10^8	1.0×10^6–1.66×10^9	7.28×10^{-11}	3.80×10^{-8}	1.00×10^{-16}–3.70×10^{-7}	5.36 (2–10)	10.0% ($N = 5$)	$$	60, 64, 68–70, 87 and 152
TA (9 and 9)	1.58×10^8	1.4×10^8	3.83×10^6–1.0×10^9	3.46×10^{-10}	7.9×10^{-10}	6.6×10^{-14}–1.20×10^{-4}	3.74 (1–10)	9.6% ($N = 5$)	$$	90, 117–119, 142, 145 and 169–173
SA (10 and 10)	2.55×10^7	3.10×10^7	5.00×10^4–1.00×10^{10}	2.50×10^{-9}	1.00×10^{-9}	1×10^{-13}–(0.0001)	2.34 (0.9–10.6)	9.4% ($N = 4$)	$	51, 52, 74, 82, 85, 141, 146, 149, 161, 167, 168 and 174–176

[a] EBL – electron beam lithography; NSL – nanosphere lithography; TA – template assisted; SA – self-assembly.

nm) and NSL (5.36 nm). The low gap distance of nanostructures made by self-assembly can be attributed to the role of linker molecules, which promote the formation of nanogaps and dictate the final gap distance. As for ordered nanofabrication techniques, the gap distance is limited only by the capabilities of the instrument and methodology.

In addition, the average and median enhancement factors for ordered techniques are only 1–2 orders of magnitude higher than those for self-assembly. For instance, NSL and template-assisted methods produce nanostructures with average EFs of 7.9×10^7 and 1.58×10^8 and median EFs of 1.0×10^8 and 1.4×10^8, respectively, whereas nanostructures formed by self-assembly produce EFs of 2.6×10^8 on average, with a median EF of 3.1×10^7. EBL also produces results close to those of ordered nanofabrication techniques in terms of EFs (average – 1.2×10^8; median – 4.6×10^8). This slight difference in enhancement factors can be explained by the formation of more ordered substrates with hot spots by lithography and template-assisted methods compared to the unstructured fabrication by self-assembly. Nevertheless, self-assembly produces a high number of nanogaps with smaller sizes, which negates its less structured nature. Moreover, if we compare the average LODs for nanostructures produced by these methods, we can observe that the difference in performance between structured and unstructured techniques is only around 1 to 2 orders of magnitude. In particular, self-assembly has a higher average LOD than the template-assisted method and about 2 orders higher LOD than EBL (2.50×10^{-9} *vs.* 3.46×10^{-10} and 1.40×10^{-11}), respectively. And in terms of median LOD, self-assembly is slightly worse performing as well compared to EBL and template-assisted methods (1.0×10^{-9} *vs.* 1.0×10^{-10}) but the median LOD for self-assembly is close to the median LOD of template-assisted methods (10×10^{-10} *vs.* 7.9×10^{-10}, respectively). Overall, EBL-based publications report the lowest average and median LODs of 1.40×10^{-11} and 1.0×10^{-10}. As for the reproducibility of these methods, all methods except EBL have an average relative standard deviation of Raman intensity between 9 and 10%, as seen in Table 2 (no reproducibility data are available for EBL). Overall, self-assembly produces comparable levels of enhancement, sensitivity, and reproducibility in contrast to structured techniques, while retaining better cost-efficiency, complexity, and scalability. We also have investigated the correlation between all parameters, including the EF, LOD, gap size, and year of publication for all 50 presented articles and found no distinguishable trends or significant relationships among them (with all R^2 values below 0.1), suggesting that these factors may have little to no identifiable dependency on each other.

Direct detection in nanogaps

Label-free SERS experiments have been carried out on a wide range of biological species, including amino acids, peptides, purine and pyrimidine bases, proteins, DNA, RNA, chlorophylls and other pigments, molecules containing chromophores (such as heme-containing proteins), stimulating drugs, and anti-tumor drug interactions with DNA and bacteria, with high sensitivity even at the single-molecule level.[177–180] This section of this review will provide an overview, albeit not thorough, of many different uses of label-free SERS with nanostructures involving nanogaps.

SERS has been used notably for the detection of different types of cancer in the last decade. For example, Au nanowires (NWs) on the sapphire surface were used for the sensitive detection of HeLa cancer cells with concentrations as low as 0.2 cell per ml.[88] These nanogap-rich AuNWs were synthesized by depositing AuNPs on vertical Au NWs, which resulted in nanogaps with a sub-10 nm size. Tian *et al.* recently developed a novel substrate with aluminum nanocrystal aggregates capable of substantial near-infrared SERS enhancements.[181] They proposed these novel low-cost SERS substrates as the first to quantitatively detect ssDNA, with no modification to either the ssDNA or the substrate surface.

Also, the direct SERS detection of simpler biologically active molecules is possible with the right nanostructure. As an example, Dinish *et al.* showcased the detection of glucose by using a nanogap substrate fabricated by deep UV photolithography.[182] This nanostructure was able to sense in a linear fashion glucose concentrations between 5 and 25 mM and produced an EF of up to 10^{11}. Detection of similar small-molecule urea was presented in a study by Wu *et al.*[127] The Au-coated plasmonic nanodome array that they utilized showed an EF of 8.51×10^7 with sub-10 nm nanogaps. And the LOD for detection of urea was calculated to be 11.9 mM. More dangerous substances were detected by Ma *et al.* and Zhang *et al.* groups [72,183] The latter group used core–shell gold nanorods for quantitative detection of polyaromatic hydrocarbons (PAHs), which can be seen in Fig. 12.[183] The resulting nanostructure contained 2–6 nm sized nanogaps and exhibited a linear response for the increasing concentrations of PAHs. And Ma *et al.* showed 10 ppb methamphetamine detection using gold nanoparticle aggregates self-assembled at different interfaces.[72]

A SERS active substrate of 60–80 nm diameter Ag nanocrystals built on Ag nanospheres was used to analyze harmful bacteria; the Raman signal was collected from cells containing as few as 10 colony-forming units per mL (CFU per mL) of three

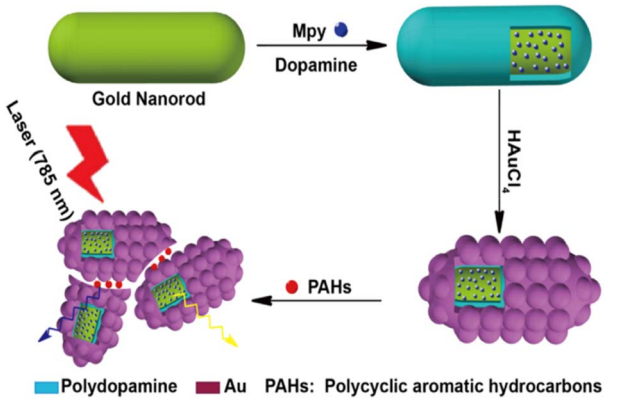

Fig. 12 Schematic illustration of the synthesis of the plasmonic core–shell structure, based on GNRs, for quantitative SERS analysis of PAHs. Reproduced under Creative Commons License from an open-access Zhang *et al.* 2018 article.[183]

important pathogens (*Escherichia coli* O157, *Salmonella typhimurium*, and *Staphylococcus aureus*). Based on the high signal amplification of 2.47×10^7, SERS spectra allowed them to identify them and determine whether the bacteria were alive or dead.[184] Recently, silver–gold bimetallic nanogap-rich SERS substrates were developed and tested to demonstrate the possibility of distinguishing Listeria monocytogenes bacteria at the strain level, by determining whether they belong to different or a single geno-sero group, in order to determine the bacterium's level of hazard.[185]

Indirect detection in nanogaps

In this section, we will discuss applications of nanogap nanostructures employing SERS tags as substrates for the indirect detection of DNA, miRNA, cell biomarkers, proteins, and molecules. Detection of DNA sequences provides important information for a variety of applications, including disease diagnosis, identification of mutations in genes, and detection of pathogens and viral strains. Current DNA detection methods include PCR and fluorescence, which have limited multiplexing capability and are prone to contamination issues. SERS-based DNA biosensors offer high sensitivity with low sample concentrations, thereby eliminating the need for amplification and potential contamination issues.[186]

An example of miRNA detection was presented by Zhou *et al.*[187] They used a bacteria template-mediated approach for the synthesis of hollow silver microspheres (Ag-HMSs), which were linked to Raman dye-containing gold nanobridged nanogap particles (Au-RNNPs). The resulting immunoassay of miRNA showed an LOD of 10 fM and EF of 10^9. Guven *et al.* developed a direct and sandwich-based assay to sensitively detect miRNAs, targeting specifically miR-21, a biomarker that is overexpressed in several cancers.[188] In the direct detection method, the authors developed a substrate consisting of gold nanorods immobilized on a gold substrate and hybridized with the target miR-21 probes. In the sandwich method, the target miR-21 was captured by a target probe functionalized on a gold slide. It was then hybridized with a second miR-21 probe that was immobilized on gold nanorods containing the reporter 5,5′-dithiobis(2-nitrobenzoic acid) (DTNB). Both assays were found to offer quick and sensitive detection of miR-21 with detection limits for the direct and sandwich assay at 0.36 and 0.85 nM, respectively.

Kang *et al.* used an Au nanoparticle-on-wire system with nanogaps, employing probe, target, and reporter DNAs to detect four pathogenic bacterial DNA strands from clinical samples in patients.[189] They were able to isolate pathogenic DNA (*Enterococcus faecium*, *Staphylococcus aureus*, *Stenotrophomonas maltophilia*, and *Vibrio vulnificus*) from various clinical specimens and achieved a low detection limit of 10 pM. Zhou *et al.* used terminal deoxynucleotidyl transferase (TdT)-catalyzed DNA with core–shell nanoparticles to alter the intraparticle gap distance and to quantitatively detect *Escherichia coli* O157:H7 (*E. coli* O157:H7) cells.[190] They achieved a limit of detection of 2 colony-forming units per ml and average recoveries of 98.1% and 105.2% in real-life samples. These examples demonstrate that SERS biosensors can be used for the diagnosis of clinical pathogens.

Proteins are important in numerous biological functions, including accelerating metabolic pathways, cell communication, and immunological response. The ability to detect and quantify certain protein markers is useful for illness diagnosis and comprehension. Human chorionic gonadotropin (hCG) for pregnancy and prostate-specific antigen (PSA) for prostate cancer are two examples of protein biomarkers that indicate health status.[186] Immunoassays are the most commonly used technique to detect proteins that are based on the specificity of antigen–antibody interaction or protein–aptamer recognition. Several SERS-based immunoassays have been developed in recent years to detect proteins. The Porter group developed a simple SERS sandwich-like immunoassay to detect a pancreatic cancer biomarker, MUC4.[191] They designed a nanochip consisting of gold nanoparticles functionalized with MUC4 antibody, which could extract and concentrate antigens from solution. SERS tags with a Raman reporter were then added on top, giving rise to intense SERS signals. This technique proved to be a simple diagnostic test for detecting MUC4 from clinical serum samples of patients. With a similar methodology, our group used an immunoassay procedure with commercially available substrates for the detection of hIgG.[168] Our study showed the possible application of a Si wafer as a possible replacement for expensive plasmonic metal substrates.

Agglomeration and association of nanotags on the substrate's surface may have a significant impact on the reproducibility and strength of the SERS signal in the sandwich SERS immunoassay.[192] Post-immunoassay characterization with SEM images has demonstrated a large degree of association for nanotags on the surface of the substrate, in some cases exceeding 50%, which implies that the impact of the nanotag association on the signal should be significant.[193,194] There were no direct and accurate measurements of the gap distances in those SEM images on the substrate's surface; however, the method of AFM/Raman and SEM/Raman map combinations, described earlier by Arbuz *et al.*, allows for the quantification of the Raman signal from individual nanotag species (single nanotags, dimers, trimers, *etc.*).[52] Previously, Sergiienko *et al.* determined that the average SERS enhancement factor for the nanotag dimer ($EF_{dimer} \approx 4 \times 10^5$) is about 1.2–1.3 times greater than that for a single nanotag.[51] Overall, there is strong potential for the SEM/Raman map combination to obtain a signal-to-structure relationship for individual nanostructures. This information might be applied to study and elucidate the impacts of the substrate effects, of nanotag-substrate separation, and of other parameters controlling the SERS signal in sandwich SERS immunoassay or in other indirect SERS assays used for the detection of biomolecules, such as relatively new methods like the aptamer-based SERS assay.[195] There are a few other examples where nanogap-rich substrates are efficient in the indirect SERS detection of biomarkers, like detection of proteinurea on gold nanoparticles over a gold film, where most nanoparticles were associated/agglomerated into dimers, trimers or oligomers.

Table 3 SEF studies involving nanogaps[a]

Year, author	Nanostructure	Preparation	Gap width (nm)	Analyte	LOD (M)	EF
2008, Bek *et al.*[213]	AuNP-FS-AuNP sandwich	AFM manipulation	40	Fluorescent polystyrene beads	NA	5.35
2010, Fu *et al.*[214] (*)	Nanopetals in a shape memory polymer substrate	Sputter-deposition of gold and silver	110	Fluorescein	NA	4000
2011, Gill *et al.*[215]	Dye-labeled DNA aggregated AgNPs	Co-aggregation process induced by the polycationic molecule spermine	1.5	Dye-DNA	NA	377.5
2012, Li *et al.*[216]	Cy5-functionalized silver nanoparticles (AgNPs)	Laboratory-designed tags and a fluorescence enhancement solution	1	IgE	1.25×10^{-12} (0.25 ng ml^{-1})	25
2012, Zhou *et al.*[217]	Disk-coupled dots-on-pillar antenna array (D2PA)	Nanoimprint (top-down) with self-aligned self-assembly (bottom-up)	5.5	IgG	3.00×10^{-16}	7400
2013, Fu *et al.*[218]	Silver nanoparticles and a silver island film (SIF)	Layer-by-layer (LBL) deposition	7.5	DiI	NA	100
2013, Punj *et al.*[219]	Plasmonic 'antenna-in-box' platform	Thermal evaporation	26	Alexa 647	NA	1100
2015, Kinoshita *et al.*[220]	Raspberry-shaped organic/inorganic hybrid structure	Anionic species doping	5	Fluorescein; rhodamine	NA; NA	10; 10
2015, Zhang *et al.*[221]	Plasmon coupled gold nanorod dimer fixed on a DNA origami nanobreadboard	Seed-mediated method	16.05	ATTO-655	NA	295
2016, Regmi *et al.*[222]	All-dielectric nanoantennas based on silicon dimers	Electron beam lithography and reactive ion etching	20	Alexa 647	NA	270
2017, Flauraud *et al.*[223]	Large flat surface arrays of in-plane nanoantennas	Planarization, etch back, and template stripping	10	Alexa 647	NA	55 000
2017, Hohenberger *et al.*[224]	Nanostructured silver films	Dewetting of thin metallic films of elemental silver	30	R6G	NA	21
2019, Yanagawa *et al.*[225] (*)	Au nanorods	Sputter-deposition of gold	47.5	Influenza virus nucleoprotein	1.00×10^{-8}	300
2019, Shang *et al.*[226]	Ag-decorated dragonfly wings (DWs)	Magnetron sputtering	40	R6G	NA	1533
2019, Pang *et al.*[227]	Au nanohole-disc arrays (Au-NHDAs)	Nanosphere lithography	10	AlexaFluor 790	NA	400
2019, Guo *et al.*[140]	AuNPs	Micro-nanomachining technology	1	CV	1.00×10^{-20}	NA
2020, Wei *et al.*[228]	Aluminum (al) nanosphere dimer	NA	1	NA	NA	34 000
2020, Dong *et al.*[229]	Tin dendrite nanostructures	*In situ* chemical reaction between $SnCl_2$ solution and Al	NA	R6G	1.00×10^{-9}	29.81
2020, Pan *et al.*[212]	SiO_2–Ag-cicada wing	Magnetron sputtering	23.75	R6G	1.00×10^{-6}.49	1.61
2020, Cruz *et al.*[230]	Plasmonically enhanced D4 (PED4)	Gap size is controlled by using a POEGMA brush	20	B-type natriuretic peptide	5.77×10^{-12} (0.02 ng ml^{-1})	100
2021, Kim *et al.*[231]	Plasmonic nanoantenna array (PNAA)	Deposition of a silver (Ag) layer on an ultraviolet (UV) nanoimprinted nanodot array	NA	Streptavidin-Cy5	NA	22

Table 3 (*Contd.*)

Year, author	Nanostructure	Preparation	Gap width (nm)	Analyte	LOD (M)	EF
2021, Lu *et al.*[232]	Ag nanorods on a micropost array (AgNMPA)	Glancing angle deposition (GLAD)	NA	MPIF-1	6.51×10^{-13} (7.8125 pg ml^{-1})	71
2021, Kim *et al.*[233]	Two AuNPs attached by a DNA origami pillar	The flexible DNA origami design	2.5	Fluorescent dye molecule	2.50×10^{-5}	5000
2023, Roy *et al.*[234]	Resonant nanogap antennas with rhodium nanocube dimers	Seeded growth, ligand exchange	10	Streptavidin and hemoglobin proteins	NA	120 (Hb)
2023, Wang *et al.*[235]	Densely packed gold nanogap arrays	Two-step anodization method; two-round electron-beam shadow deposition	6, 7	Cyanine dye	NA	10 000
2025, Wu *et al.*[154] (*)	Wafer-scale plasmonic metamaterial sheet (PLAMS)	Spin-coating, plasma treatment, RIE, e-beam evaporation metal deposition, and ICP-CVD	≥1	IR-780 iodide; Nile blue; rhodamine 6G	NA	209; 106; 46

Average gap (nm)	Median gap (nm)	Average LOD (M)	Median LOD (M)	Average EF	Median EF
9.41	10	1.01×10^{-11}	5.77×10^{-12}	220.89	164.5

Average gap (nm)	Median gap (nm)	Average LOD (M)	Median LOD (M)	Average EF	Median EF
7.75	10	4.29×10^{-12}	3.51×10^{-12}	212.9	164.5

[a] We also decided to do the same statistical calculations excluding the papers where the gap is > 40 nm (excluded articles are noted with an asterisk sign).

Li *et al.* attached Raman dyes and methoxy poly(ethylene glycol) thiol (mPEG-SH) to gold nanoparticles (AuNPs) to prepare gold cores.[132] Next, the Ag nanoparticles were deposited on the gold core, followed by etching of the subsequent Ag shell in order to form an interior nanogap. This nanostructure was then examined by detecting PSA and C-reactive protein (CRP), which are biomarkers for prostate cancer and coronary diseases, respectively. The LOD for these two biomarkers was well below the diagnostic concentrations of these diseases. In addition, this nanostructure was applied in cancer cell imaging and was able to qualitatively show CCRF-CEM cells, which are precursors for T cell acute lymphoblastic leukemia.

Xu *et al.* were able to detect three disease biomarkers simultaneously using a SERS substrate.[196] They employed self-assembled silver nanoparticle pyramids on a SERS active substrate with 2–8 nm sized nanogaps and SERS tags to detect the biomarkers PSA, thrombin, and mucin-1 simultaneously. They used DNA aptamers for target recognition and were able to achieve detection at the attomolar concentration of proteins. With this biosensor, the LODs for the three biomarkers, PSA, thrombin, and mucin-1, were 0.96, 85, and 9.2 aM, respectively.

SEF in nanogaps

This effect was first observed and discovered in the late 1960s by Drexhage during investigations on the fluorescence lifetime in the presence of a metal film.[197,198] In the next several decades, this topic gained more attention, mostly due to the substantial research studies by the group of Lakowicz and Geddes.[199–202] The most popular substrate of choice at that time was silver island films (SiFs).[28,203,204] Then the potential use of nanoparticles was revealed, especially silver, gold, and core–shell nanoparticles.[205–207] Nowadays, the use of quantum dots and biochips for SEF is becoming increasingly popular.[208–211] Consequently, with the development of the new metallic surfaces and nanostructures, the possible applications of MEF are steadily increasing.[236] Despite all these innovations, the signal enhancement of this spectroscopic technique is heavily influenced by the appearance of hot spots, which are primarily found in nanogaps between plasmonic metals. Thus, the application of these nanostructures in SEF is a prominent topic of study. And it is evident from the literature search that its development is far from its potential. A fraction of this area of research is summarized in Table 3. In this table only reports with relatively well-structured SEF substrates are reviewed. A few publications where large (up to several 100s) SEF enhancement is achieved on less structured/controlled substrates are NOT included in the table. For instance, it is the case for some biological analytes such as bacterial cells labelled with composite core shell quantum dots or carbon dots on metallic substrates, particularly gold and aluminum films[237–239] In addition to that, H. Chowdhury *et al.* calculated the theoretical EF for an aluminum nanoparticle dimer system which can be higher than 3500-fold, but in this table we consider only experimental results.[240]

One of the examples of nanogap application in SEF, which is included in the table, is demonstrated in the work of Li *et al.*, where they used a Cy-5 oligomer tag as a linker between two colloidal silver nanoparticles.[216] The performance of this nanostructure was explored by detection of IgE in the concentration range of 0.5 ng ml^{-1} – 16 ng ml^{-1}. The LOD for this measurement was calculated to be 0.25 ng ml^{-1}. An approach involving the top-down nanoimprint technique and bottom-up self-assembly for fabrication of nanogap arrays for SEF was presented by Zhou *et al.*[217] The resulting plasmonic nanostructure was further utilized for immunoassay detection of hIgG and showed a 3×10^6 increase in sensitivity compared to identical assay on the glass surface. The fluorescence enhancement was calculated to be 4×10^6 and the LOD was 0.9×10^{-9} M. According to Punj *et al.*, even single-molecular SEF detection was possible by utilizing a nanogap containing an "antenna-in-box" plasmonic nanostructure,[219] with detection

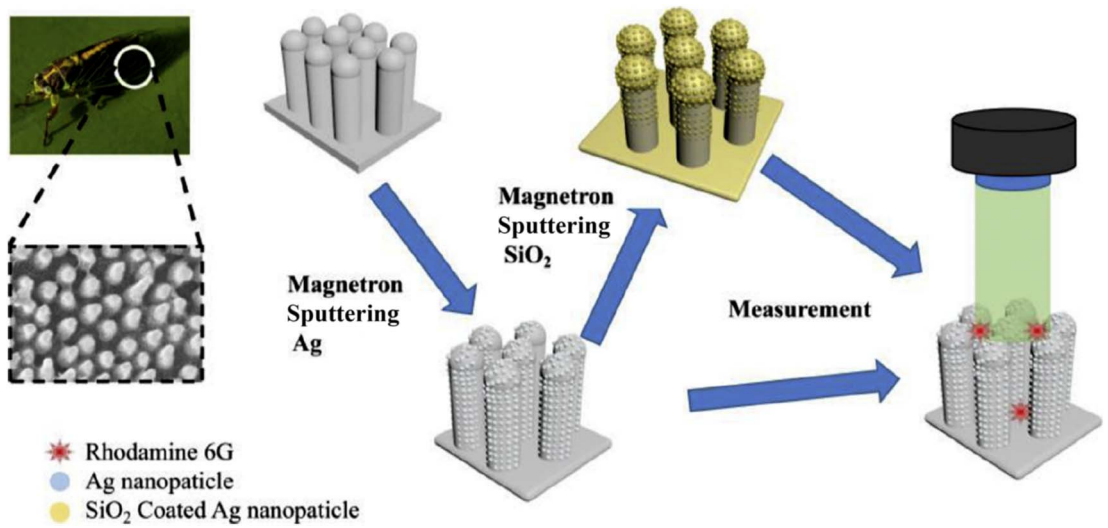

Fig. 13 Schematic diagram of the Ag-X substrate fabrication process and SEF measurement using the fluorescent system. Reproduced with permission granted by Elsevier B.V. from the Pan *et al.* 2020 article.[212]

volumes reaching 50 zeptoliters and fluorescence enhancement of 1100. In addition, Yanagawa *et al.* showed the detection of influenza virus protein by using gold nanorods on a template substrate.[225] The subsequent immunoassay for virus protein showed that even a 10 nM concentration of nanoparticles can detect the virus protein antigen. A more exotic approach for nanogap fabrication was proposed by Pan *et al.*[212] They used cicada wings as a template for magnetron sputtering of silver nanoparticles, the process for which can be seen in Fig. 13. The final 3D nanostructure possessed nanogaps with distances between 7 and 40 nm and was used for quantitative detection of R6G. The measurement of R6G in the concentration range from 10 mM to 100 nM showed a LOD of 3.24×10^{-7} M.

There are also emerging examples of application of combined SERS/SEF techniques in sensing. While SERS provides the ability for multiplexing and exceptionally sensitive detection, SEF offers rapid fluorescence imaging. The combination of these surface-enhanced techniques is beneficial for sensing, as it improves sensitivity and accuracy.[241] For instance, Tatar *et al.* developed a SERS/SEF dual-mode sensing platform based on PVP-coated gold nanostar films deposited on polystyrene plates.[242] Polyvinylpyrrolidone-stabilized nanostars demonstrated reduced quenching compared to unmodified ones and hence better SEF performance. This dual-mode platform reached an EF of 3.2×10^5 with Rh800 as an analyte. Previously, PVP was also used to optimize the SEF properties of other nanostructures, such as quantum dots embedded in a PVP matrix on polystyrene microplastics, as reported by Falamas *et al.* where this polymer was used for improving dispersion of QDs, which led to a more consistent and reproducible SEF signal.[243] Typically, combining SERS and SEF is impeded by the fact that surface-enhanced fluorescence requires a dielectric spacer to prevent fluorescence quenching; however, their use weakens the electromagnetic hotspots required for SERS. Nonetheless Kaiyu Wu's research group developed a wafer-scale plasmonic metamaterial sheet that maximized both SERS's and SEF's surface-average enhancement factors (achieving corresponding EFs of 1.17×10^6 for SERS and 209 for SEF, respectively).[154] The platform was capable of rapid target screening *via* SEF followed by highly sensitive and specific molecular characterization using SERS. Further morphological improvements and implementation of nanogaps in substrates might enhance the analytical performance of dual-sensing systems in the future, allowing these dual-mode SERS/SEF substrates to be used in other sensing-related fields as well.

Conclusions

In this review, we presented and discussed the scope of use and importance of nanogaps in surface-enhanced spectroscopies, starting from the theoretical background and going through fabrication methodologies to the published applications of these nanostructures in direct and indirect SERS sensing. Also, we discussed SEF as a surface-enhanced technique that is also dependent on nanogap enhancement.

The fabrication techniques depicted in this review are just a tip of the actual iceberg of innovations made in this area. When these techniques are compared in terms of their EFs, the SERS substrates fabricated with ordered nanofabrication techniques such as EBL and NSL as reported in Table 2, which is based on a total of 38 studies, tentatively produce EFs, which are only up to one order of magnitude higher (for EBL) than SERS EFs observed on substrates fabricated with self-assembly (SA), when median reported EFs are 5×10^8 *vs.* 3×10^7 for EBL *vs.* SA respectively. Moreover, the difference in performance becomes less evident when LOD values are compared. When these techniques are compared in terms of LOD, substrates fabricated by EBL demonstrated only one order of magnitude better LOD/higher sensitivity in comparison to the substrates fabricated by self-assembly with a median reported LOD of 0.1 nM *vs.* 1 nM respectively.

Since unstructured nanofabrication processes are less expensive, have lower complexity, and are more scalable than structured techniques, self-assembly is likely to be a more efficient technique for the fabrication of nanostructures applied in surface-enhanced spectroscopy based on its performance-to-cost ratio.

When these techniques are compared in terms of their figures of merit, the ordered nanofabrication techniques reported in the reviewed studies typically produce EFs up to one order of magnitude higher than EFs of self-assembly. Moreover, the difference in performance becomes less evident when comparing LODs and reproducibility values overall.

The variations and combinations of different methodologies enable the synthesis of nanogaps for a myriad of applications, starting from metal ion detection to bacteria and virus sensing, although the challenges of scalability, stability, and reproducibility affecting these techniques are major obstacles for the broad commercialization of these nanostructures and SERS as a whole. A similar image can be seen for the real-life applicability of the SEF technique. But the recent breakthroughs in these research areas show great promise for the potential real-life use of these techniques.

Author contributions

Alisher Sultangaziyev: major contribution to writing the original draft, visualization, formal analysis; Dinmukhamed Aliyev: writing the original draft, formal analysis; Ansar Seitkali writing the final draft and editing, formal analysis; Rostislav Bukasov: conceptualization, management, funding, writing the final draft and editing, formal analysis.

Conflicts of interest

There are no conflicts of interest to declare.

Data availability

No original experimental data is generated or reported in this review paper. The data in this review article is included in the paper and is collected from original publications referenced in the paper.

Notes and references

1 M. Fleischmann, P. J. Hendra and A. J. McQuillan, *Chem. Phys. Lett.*, 1974, **26**, 163–166.
2 M. G. Albrecht and J. A. Creighton, *J. Am. Chem. Soc.*, 1977, **99**, 5215–5217.
3 D. L. Jeanmaire and R. P. Van Duyne, *J. Electroanal. Chem. Interfacial Electrochem.*, 1977, **84**, 1–20.
4 E. Hutter and J. H. Fendler, *Adv. Mater.*, 2004, **16**, 1685–1706.
5 K. C. Bantz, A. F. Meyer, N. J. Wittenberg, H. Im, Ö. Kurtuluş, S. H. Lee, N. C. Lindquist, S.-H. Oh and C. L. Haynes, *Phys. Chem. Chem. Phys.*, 2011, **13**, 11551–11567.
6 E. C. Le Ru, C. Galloway and P. G. Etchegoin, *Phys. Chem. Chem. Phys.*, 2006, **8**, 3083–3087.
7 R. Pilot, R. Signorini, C. Durante, L. Orian, M. Bhamidipati and L. Fabris, *Biosensors*, 2019, **9**, 57.
8 P. L. Stiles, J. A. Dieringer, N. C. Shah and R. P. Van Duyne, *Annu. Rev. Anal. Chem.*, 2008, **1**, 601–626.
9 B. Sharma, R. R. Frontiera, A.-I. Henry, E. Ringe and R. P. Van Duyne, *Mater. Today*, 2012, **15**, 16–25.
10 G. Wang, H.-Y. Park, R. J. Lipert and M. D. Porter, *Anal. Chem.*, 2009, **81**, 9643–9650.
11 S. Schlucker, *Angew. Chem., Int. Ed.*, 2014, **53**, 4756–4795.
12 D. Radziuk and H. Moehwald, *Phys. Chem. Chem. Phys.*, 2015, **17**, 21072–21093.
13 A. J. Driscoll, M. H. Harpster and P. A. Johnson, *Phys. Chem. Chem. Phys.*, 2013, **15**, 20415–20433.
14 J. B. Song, P. Huang, H. W. Duan and X. Y. Chen, *Acc. Chem. Res.*, 2015, **48**, 2506–2515.
15 L. A. Lane, X. M. Qian and S. M. Nie, *Chem. Rev.*, 2015, **115**, 10489–10529.
16 D. S. Grubisha, R. J. Lipert, H. Y. Park, J. Driskell and M. D. Porter, *Anal. Chem.*, 2003, **75**, 5936–5943.
17 R. A. Halvorson and P. J. Vikesland, *Environ. Sci. Technol.*, 2010, **44**, 7749–7755.
18 S. Nie and S. R. Emory, *Science*, 1997, **275**, 1102–1106.
19 K. Kneipp, Y. Wang, H. Kneipp, L. T. Perelman, I. Itzkan, R. R. Dasari and M. S. Feld, *Phys. Rev. Lett.*, 1997, **78**, 1667–1670.
20 J. P. Camden, J. A. Dieringer, Y. Wang, D. J. Masiello, L. D. Marks, G. C. Schatz and R. P. Van Duyne, *J. Am. Chem. Soc.*, 2008, **130**, 12616–12617.
21 R. Zhang, Y. Zhang, Z. C. Dong, S. Jiang, C. Zhang, L. G. Chen, L. Zhang, Y. Liao, J. Aizpurua, Y. Luo, J. L. Yang and J. G. Hou, *Nature*, 2013, **498**, 82–86.
22 H. S. Rye, J. M. Dabora, M. A. Quesada, R. A. Mathies and A. N. Glazer, *Anal. Biochem.*, 1993, **208**, 144–150.
23 A. Jablonski, *Nature*, 1933, **131**, 839–840.
24 S. J. Strickler and R. A. Berg, *J. Chem. Phys.*, 1962, **37**, 814–822.
25 G. W. Ford and W. H. Weber, *Phys. Rep.*, 1984, **113**, 195–287.
26 R. R. Chance, A. H. Miller, A. Prock and R. Silbey, *J. Chem. Phys.*, 1975, **63**, 1589–1595.
27 M. Moskovits, *Rev. Mod. Phys.*, 1985, **57**, 783–826.
28 E. G. Matveeva, Z. Gryczynski and J. R. Lakowicz, *J. Immunol. Methods*, 2005, **302**, 26–35.
29 A. Wokaun, in *Solid State Physics*, ed. H. Ehrenreich, D. Turnbull and F. Seitz, Academic Press, 1984, vol. 38, pp. 223–294.
30 C. D. Geddes, H. Cao, I. Gryczynski, Z. Gryczynski, J. Fang and J. R. Lakowicz, *J. Phys. Chem. A*, 2003, **107**, 3443–3449.
31 Y. Jeong, Y.-M. Kook, K. Lee and W.-G. Koh, *Biosens. Bioelectron.:X*, 2018, **111**, 102–116.
32 H. Xu, J. Aizpurua, M. Käll and P. Apell, *Phys. Rev. E*, 2000, **62**, 4318–4324.
33 S.-Y. Ding, E.-M. You, Z.-Q. Tian and M. Moskovits, *Chem. Soc. Rev.*, 2017, **46**, 4042–4076.
34 J. Jiang, K. Bosnick, M. Maillard and L. Brus, *J. Phys. Chem. B*, 2003, **107**, 9964–9972.
35 M. J. Banholzer, J. E. Millstone, L. Qin and C. A. Mirkin, *Chem. Soc. Rev.*, 2008, **37**, 885–897.
36 M. Moskovits, *J. Raman Spectrosc.*, 2005, **36**, 485–496.
37 D. Cialla, A. März, R. Böhme, F. Theil, K. Weber, M. Schmitt and J. Popp, *Anal. Bioanal. Chem.*, 2012, **403**, 27–54.
38 R. M. Jarvis, H. E. Johnson, E. Olembe, A. Panneerselvam, M. A. Malik, M. Afzaal, P. O'Brien and R. Goodacre, *Analyst*, 2008, **133**, 1449–1452.
39 E. Le Ru and P. Etchegoin, *Principles of Surface-Enhanced Raman Spectroscopy: and Related Plasmonic Effects*, Elsevier, 2009.
40 J. M. McMahon, S. K. Gray and G. C. Schatz, *Phys. Rev. B:Condens. Matter Mater. Phys.*, 2011, **83**, 115428.
41 J. M. McMahon, S. Li, L. K. Ausman and G. C. Schatz, *J. Phys. Chem. C*, 2012, **116**, 1627–1637.
42 M. A. Mahmoud and M. A. El-Sayed, *Nano Lett.*, 2009, **9**, 3025–3031.
43 W. Zhu, R. Esteban, A. G. Borisov, J. J. Baumberg, P. Nordlander, H. J. Lezec, J. Aizpurua and K. B. Crozier, *Nat. Commun.*, 2016, **7**, 11495.
44 G. Hajisalem, M. S. Nezami and R. Gordon, *Nano Lett.*, 2014, **14**, 6651–6654.
45 S. L. Kleinman, R. R. Frontiera, A. I. Henry, J. A. Dieringer and R. P. Van Duyne, *Phys. Chem. Chem. Phys.*, 2013, **15**, 21–36.
46 E. C. Le Ru, P. G. Etchegoin and M. Meyer, *J. Chem. Phys.*, 2006, **125**, 204701.
47 J. M. McMahon, A.-I. Henry, K. L. Wustholz, M. J. Natan, R. G. Freeman, R. P. Van Duyne and G. C. Schatz, *Anal. Bioanal. Chem.*, 2009, **394**, 1819–1825.
48 K. L. Wustholz, A.-I. Henry, J. M. McMahon, R. G. Freeman, N. Valley, M. E. Piotti, M. J. Natan, G. C. Schatz and R. P. Van Duyne, *J. Am. Chem. Soc.*, 2010, **132**, 10903–10910.
49 W. Li, P. H. Camargo, L. Au, Q. Zhang, M. Rycenga and Y. Xia, *Angew Chem. Int. Ed. Engl.*, 2010, **49**, 164–168.
50 D. Steinigeweg, M. Schuetz and S. Schluecker, *Nanoscale*, 2013, **5**, 110–113.
51 S. Sergiienko, K. Moor, K. Gudun, Z. Yelemessova and R. Bukasov, *Phys. Chem. Chem. Phys.*, 2017, **19**, 4478–4487.
52 A. Arbuz, A. Sultangaziyev, A. Rapikov, Z. Kunushpayeva and R. Bukasov, *Nanoscale Adv.*, 2022, **4**, 268–280.

53 S. S. Masango, R. A. Hackler, N. Large, A.-I. Henry, M. O. McAnally, G. C. Schatz, P. C. Stair and R. P. Van Duyne, *Nano Lett.*, 2016, **16**, 4251–4259.
54 N. E. Marotta, K. R. Beavers and L. A. Bottomley, *Anal. Chem.*, 2013, **85**, 1440–1446.
55 X.-M. Lin, Y. Cui, Y.-H. Xu, B. Ren and Z.-Q. Tian, *Anal. Bioanal. Chem.*, 2009, **394**, 1729–1745.
56 M. J. Natan, *Faraday Discuss.*, 2006, **132**, 321–328.
57 Y. Yu, T.-H. Xiao, Y. Wu, W. Li, Q.-G. Zeng, L. Long and Z.-Y. Li, *Adv. Photonics*, 2020, **2**, 014002.
58 X. Wang, X. Zhu, H. Shi, Y. Chen, Z. Chen, Y. Zeng, Z. Tang and H. Duan, *ACS Appl. Mater. Interfaces*, 2018, **10**, 35607–35614.
59 H. Im, K. C. Bantz, N. C. Lindquist, C. L. Haynes and S.-H. Oh, *Nano Lett.*, 2010, **10**, 2231–2236.
60 H. Cai, Q. Meng, H. Zhao, M. Li, Y. Dai, Y. Lin, H. Ding, N. Pan, Y. Tian, Y. Luo and X. Wang, *ACS Appl. Mater. Interfaces*, 2018, **10**, 20189–20195.
61 H. Cai, Y. Wu, Y. Dai, N. Pan, Y. Tian, Y. Luo and X. Wang, *Opt. Express*, 2016, **24**, 20808–20815.
62 Y.-Q. Cao, K. Qin, L. Zhu, X. Qian, X.-J. Zhang, D. Wu and A.-D. Li, *Sci. Rep.*, 2017, **7**, 1–8.
63 M. Liu, L. Sun, C. Cheng, H. Hu, Z. Shen and H. J. Fan, *Nanoscale*, 2011, **3**, 3627–3630.
64 X. Li, Y. Zhang, Z. X. Shen and H. J. Fan, *Small*, 2012, **8**, 2548.
65 J. Zhang, M. Irannejad and B. Cui, *Plasmonics*, 2015, **10**, 831–837.
66 L. Lesser-Rojas, P. Ebbinghaus, G. Vasan, M.-L. Chu, A. Erbe and C.-F. Chou, *Nano Lett.*, 2014, **14**, 2242–2250.
67 A. W. Clark and J. M. Cooper, *Small*, 2011, **7**, 119–125.
68 Y. Wang, X. Zhao, W. Gao, L. Chen, S. Chen, M. Wei, M. Gao, C. Wang, Y. Zhang and J. Yang, *RSC Adv.*, 2015, **5**, 7454–7460.
69 Y. Sawai, B. Takimoto, H. Nabika, K. Ajito and K. Murakoshi, *J. Am. Chem. Soc.*, 2007, **129**, 1658–1662.
70 H. Im, K. C. Bantz, S. H. Lee, T. W. Johnson, C. L. Haynes and S.-H. Oh, *Adv. Mater.*, 2013, **25**, 2678–2685.
71 H. M. Jin, J. Y. Kim, M. Heo, S.-J. Jeong, B. H. Kim, S. K. Cha, K. H. Han, J. H. Kim, G. G. Yang, J. Shin and S. O. Kim, *ACS Appl. Mater. Interfaces*, 2018, **10**, 44660–44667.
72 Y. Ma, H. Liu, M. Mao, J. Meng, L. Yang and J. Liu, *Anal. Chem.*, 2016, **88**, 8145–8151.
73 H. Li, D. Men, Y. Sun, D. Liu, X. Li, L. Li, C. Li, W. Cai and Y. Li, *J. Colloid Interface Sci.*, 2017, **505**, 467–475.
74 V. T. Cong, E.-O. Ganbold, J. K. Saha, J. Jang, J. Min, J. Choo, S. Kim, N. W. Song, S. J. Son, S. B. Lee and S.-W. Joo, *J. Am. Chem. Soc.*, 2014, **136**, 3833–3841.
75 D. Wang, W. Zhu, M. D. Best, J. P. Camden and K. B. Crozier, *Nano Lett.*, 2013, **13**, 2194–2198.
76 Y. Zhang, Y.-R. Zhen, O. Neumann, J. K. Day, P. Nordlander and N. J. Halas, *Nat. Commun.*, 2014, **5**, 4424.
77 D.-K. Lim, K.-S. Jeon, H. M. Kim, J.-M. Nam and Y. D. Suh, *Nat. Mater.*, 2010, **9**, 60–67.
78 V. V. Thacker, L. O. Herrmann, D. O. Sigle, T. Zhang, T. Liedl, J. J. Baumberg and U. F. Keyser, *Nat. Commun.*, 2014, **5**, 3448.
79 K. Gudun, Z. Elemessova, L. Khamkhash, E. Ralchenko and R. Bukasov, *J. Nanomater.*, 2017, **2017**, 8.
80 A. Hakonen, M. Svedendahl, R. Ogier, Z.-J. Yang, K. Lodewijks, R. Verre, T. Shegai, P. O. Andersson and M. Käll, *Nanoscale*, 2015, **7**, 9405–9410.
81 G. Lu, H. Li, S. Wu, P. Chen and H. Zhang, *Nanoscale*, 2012, **4**, 860–863.
82 J. Li, T.-S. Deng, X. Liu, J. A. Dolan, N. F. Scherer and P. F. Nealey, *Nano Lett.*, 2019, **19**, 4314–4320.
83 B. Zhao, J. Shen, S. Chen, D. Wang, F. Li, S. Mathur, S. Song and C. Fan, *Chem. Sci.*, 2014, **5**, 4460–4466.
84 M. Kim, S. M. Ko, J.-M. Kim, J. Son, C. Lee, W.-K. Rhim and J.-M. Nam, *ACS Cent. Sci.*, 2018, **4**, 277–287.
85 J. Song, B. Duan, C. Wang, J. Zhou, L. Pu, Z. Fang, P. Wang, T. T. Lim and H. Duan, *J. Am. Chem. Soc.*, 2014, **136**, 6838–6841.
86 F. Shao, Z. Lu, C. Liu, H. Han, K. Chen, W. Li, Q. He, H. Peng and J. Chen, *ACS Appl. Mater. Interfaces*, 2014, **6**, 6281–6289.
87 C. Tian, Y. Deng, D. Zhao and J. Fang, *Adv. Opt. Mater.*, 2015, **3**, 404–411.
88 G. Eom, H. Kim, A. Hwang, H.-Y. Son, Y. Choi, J. Moon, D. Kim, M. Lee, E.-K. Lim, J. Jeong, Y.-M. Huh, M.-K. Seo, T. Kang and B. Kim, *Adv. Funct. Mater.*, 2017, **27**, 1701832.
89 S.-C. Cheng and T.-C. Wen, *Mater. Chem. Phys.*, 2014, **143**, 1331–1337.
90 Q. Hao, H. Huang, X. Fan, Y. Yin, J. Wang, W. Li, T. Qiu, L. Ma, P. K. Chu and O. G. Schmidt, *ACS Appl. Mater. Interfaces*, 2017, **9**, 36199–36205.
91 R. Liu, J.-f. Liu, X.-x. Zhou, M.-T. Sun and G.-b. Jiang, *Anal. Chem.*, 2011, **83**, 9131–9137.
92 J. Chen, G. Qin, J. Wang, J. Yu, B. Shen, S. Li, Y. Ren, L. Zuo, W. Shen and B. Das, *Biosens. Bioelectron.*, 2013, **44**, 191–197.
93 T. Siegfried, Y. Ekinci, H. H. Solak, O. J. F. Martin and H. Sigg, *Appl. Phys. Lett.*, 2011, **99**, 263302.
94 X. Lu, Y. Huang, B. Liu, L. Zhang, L. Song, J. Zhang, A. Zhang and T. Chen, *Chem. Mater.*, 2018, **30**, 1989–1997.
95 L. F. Thompson, in *Introduction to Microlithography*, American Chemical Society, 1983, ch. 1, vol. 219, pp. 1–13.
96 Z. Cui, *Course Notes*, ECE, 2008, 730.
97 A. Sarangan, *Nanofabrication: Principles to Laboratory Practice*, CRC Press, 2016.
98 R. F. Peters, L. Gutierrez-Rivera, S. K. Dew and M. Stepanova, *J. Visualized Exp.*, 2015, e52712.
99 W. Zhu, M. G. Banaee, D. Wang, Y. Chu and K. B. Crozier, *Small*, 2011, **7**, 1761–1766.
100 M. E. Stewart, C. R. Anderton, L. B. Thompson, J. Maria, S. K. Gray, J. A. Rogers and R. G. Nuzzo, *Chem. Rev.*, 2008, **108**, 494–521.
101 D. R. Ward, N. K. Grady, C. S. Levin, N. J. Halas, Y. Wu, P. Nordlander and D. Natelson, *Nano Lett.*, 2007, **7**, 1396–1400.
102 C. L. Haynes and R. P. Van Duyne, *J. Phys. Chem. B*, 2001, **105**, 5599–5611.
103 T. R. Jensen, M. D. Malinsky, C. L. Haynes and R. P. Van Duyne, *J. Phys. Chem. B*, 2000, **104**, 10549–10556.

104 D.-Y. Wu, J.-F. Li, B. Ren and Z.-Q. Tian, *Chem. Soc. Rev.*, 2008, **37**, 1025–1041.
105 P. Colson, C. Henrist and R. Cloots, *J. Nanomater.*, 2013, **2013**, 948510.
106 C. L. Haynes and R. P. Van Duyne, *J. Phys. Chem. B*, 2003, **107**, 7426–7433.
107 J. A. Dieringer, A. D. McFarland, N. C. Shah, D. A. Stuart, A. V. Whitney, C. R. Yonzon, M. A. Young, X. Zhang and R. P. Van Duyne, *Faraday Discuss.*, 2006, **132**, 9–26.
108 C. L. Haynes, A. D. McFarland, M. T. Smith, J. C. Hulteen and R. P. Van Duyne, *J. Phys. Chem. B*, 2002, **106**, 1898–1902.
109 B. Ai, Y. Yu, H. Möhwald, G. Zhang and B. Yang, *Adv. Colloid Interface Sci.*, 2014, **206**, 5–16.
110 J. S. J. Tang, R. S. Bader, E. S. A. Goerlitzer, J. F. Wendisch, G. R. Bourret, M. Rey and N. Vogel, *ACS Omega*, 2018, **3**, 12089–12098.
111 Z. Huang, H. Fang and J. Zhu, *Adv. Mater.*, 2007, **19**, 744–748.
112 J. Yeom, D. Ratchford, C. R. Field, T. H. Brintlinger and P. E. Pehrsson, *Adv. Funct. Mater.*, 2014, **24**, 106–116.
113 A. Walcarius, E. Sibottier, M. Etienne and J. Ghanbaja, *Nat. Mater.*, 2007, **6**, 602–608.
114 H. Masuda and K. Fukuda, *Science*, 1995, **268**, 1466–1468.
115 M. Fan, G. F. S. Andrade and A. G. Brolo, *Anal. Chim. Acta*, 2011, **693**, 7–25.
116 H.-H. Wang, C.-Y. Liu, S.-B. Wu, N.-W. Liu, C.-Y. Peng, T.-H. Chan, C.-F. Hsu, J.-K. Wang and Y.-L. Wang, *Adv. Mater.*, 2006, **18**, 491–495.
117 C. Tian, J. Li, C. Ma, P. Wang, X. Sun and J. Fang, *Nanoscale*, 2015, **7**, 12318–12324.
118 J. M. Baik, S. J. Lee and M. Moskovits, *Nano Lett.*, 2009, **9**, 672–676.
119 Q. Fu, Z. Zhan, J. Dou, X. Zheng, R. Xu, M. Wu and Y. Lei, *ACS Appl. Mater. Interfaces*, 2015, **7**, 13322–13328.
120 L. Guerrini and D. Graham, *Chem. Soc. Rev.*, 2012, **41**, 7085–7107.
121 J. Turkevich, P. C. Stevenson and J. Hillier, *J. Phys. Chem.*, 1953, **57**, 670–673.
122 P. C. Lee and D. Meisel, *J. Phys. Chem.*, 1982, **86**, 3391–3395.
123 V. Amendola and M. Meneghetti, *Phys. Chem. Chem. Phys.*, 2013, **15**, 3027–3046.
124 G. M. Herrera, A. C. Padilla and S. P. Hernandez-Rivera, *Nanomaterials*, 2013, **3**, 158–172.
125 D.-K. Lim, K.-S. Jeon, J.-H. Hwang, H. Kim, S. Kwon, Y. D. Suh and J.-M. Nam, *Nat. Nanotechnol.*, 2011, **6**, 452–460.
126 Y.-J. Oh and K.-H. Jeong, *Adv. Mater.*, 2012, **24**, 2234–2237.
127 H.-Y. Wu, C. J. Choi and B. T. Cunningham, *Small*, 2012, **8**, 2878–2885.
128 J.-H. Lee, M.-H. You, G.-H. Kim and J.-M. Nam, *Nano Lett.*, 2014, **14**, 6217–6225.
129 J. Shen, J. Su, J. Yan, B. Zhao, D. Wang, S. Wang, K. Li, M. Liu, Y. He, S. Mathur, C. Fan and S. Song, *Nano Res.*, 2015, **8**, 731–742.
130 M. Tabatabaei, M. Najiminaini, K. Davieau, B. Kaminska, M. R. Singh, J. J. L. Carson and F. Lagugné-Labarthet, *ACS Photonics*, 2015, **2**, 752–759.
131 J. W. Jeong, M. P. M. Arnob, K.-M. Baek, S. Y. Lee, W.-C. Shih and Y. S. Jung, *Adv. Mater.*, 2016, **28**, 8695–8704.
132 J. Li, Z. Zhu, B. Zhu, Y. Ma, B. Lin, R. Liu, Y. Song, H. Lin, S. Tu and C. Yang, *Anal. Chem.*, 2016, **88**, 7828–7836.
133 X.-H. Pham, M. Lee, S. Shim, S. Jeong, H.-M. Kim, E. Hahm, S. H. Lee, Y.-S. Lee, D. H. Jeong and B.-H. Jun, *RSC Adv.*, 2017, **7**, 7015–7021.
134 W. Zhang, P. Man, M. Wang, Y. Shi, Y. Xu, Z. Li, C. Yang and B. Man, *Carbon*, 2018, **133**, 300–305.
135 C. Yang, Y. Chen, D. Liu, C. Chen, J. Wang, Y. Fan, S. Huang and W. Lei, *ACS Appl. Mater. Interfaces*, 2018, **10**, 8317–8323.
136 R. Pan, Y. Yang, Y. Wang, S. Li, Z. Liu, Y. Su, B. Quan, Y. Li, C. Gu and J. Li, *Nanoscale*, 2018, **10**, 3171–3180.
137 G. Wu, F. Cao, P. Zhao, X. Zhang, Z. Li, N. Yu, Z. Wang, Y. Hu, H. Sun and H. Gu, *Adv. Mater. Interfaces*, 2018, **5**, 1800820.
138 J. Kwak, W. Lee, J.-B. Kim, S.-I. Bae and K.-H. Jeong, *J. Biomed. Opt.*, 2019, **24**, 037001.
139 J.-K. Yang, I.-J. Hwang, M. G. Cha, H.-I. Kim, D. Yim, D. H. Jeong, Y.-S. Lee and J.-H. Kim, *Small*, 2019, 15.
140 H. Guo, K. Qian, A. Cai, J. Tang and J. Liu, *Sens. Actuators, B*, 2019, **300**, 126846.
141 Z. Lao, Y. Zheng, Y. Dai, Y. Hu, J. Ni, S. Ji, Z. Cai, Z. J. Smith, J. Li, L. Zhang, D. Wu and J. Chu, *Adv. Funct. Mater.*, 2020, **30**, 1909467.
142 S. Adhikari, E. K. Ampadu, M. Kim, D. Noh, E. Oh and D. Lee, *Sensors*, 2021, **21**, 5567.
143 M. Shafi, R. Liu, Z. Zha, C. Li, X. Du, S. Wali, S. Jiang, B. Man and M. Liu, *Appl. Surf. Sci.*, 2021, **555**, 149729.
144 Q. Zhao, H. Yang, B. Nie, Y. Lao, J. Shao and G. Li, *ACS Appl. Mater. Interfaces*, 2022, **14**, 3580–3590.
145 S. Bock, Y.-S. Choi, M. Kim, Y. Yun, X.-H. Pham, J. Kim, B. Seong, W. Kim, A. Jo, K.-M. Ham, S. G. Lee, S. H. Lee, H. Kang, H. S. Choi, D. H. Jeong, H. Chang, D.-E. Kim and B.-H. Jun, *J. Nanobiotechnol.*, 2022, **20**, 1–12.
146 Y. Teng, X. Li, Y. Chen, P. Xu, Z. Pan, K. Shao and N. Sun, *Microchim. Acta*, 2023, **190**, 185.
147 S. Adhikari, M. Kim, J. Lee, C. Hong, Y. Jeong, J. Baek, J. H. Lee, S. Lee, J. Kim, I. Yoon, Y. Jang and D. Lee, *ACS Appl. Nano Mater.*, 2024, **7**, 14050–14056.
148 S. Lee, S. Lee, W. Park, S. Lee, S. Kwon, M. J. Oh, M. Haddadnezhad, I. Jung, B. Kim, J. Park, K. S. Shin, H. Lee, J. Yoo, W.-K. Kim and S. Park, *Nano Lett.*, 2024, **24**, 4233–4240.
149 S. M. Sibug-Torres, D.-B. Grys, G. Kang, M. Niihori, E. Wyatt, N. Spiesshofer, A. Ruane, B. de Nijs and J. J. Baumberg, *Nat. Commun.*, 2024, **15**, 2022.
150 Y.-X. Zhao, X. Liang, Y.-L. Chen, Y.-T. Chen, L. Ma, S.-J. Ding, X.-B. Chen and Q.-Q. Wang, *Anal. Chem.*, 2024, **96**, 8416–8423.
151 M. Lv, X. Wen, L. Ji, C. Chen, H. Lu, J. Hao, Y. Hu, Q. Zhang, M. Zhu, R. Wei and Q. Wang, *Microchem. J.*, 2025, **218**, 115557.

152 M. C. Suster, A. Szymańska, T. J. Antosiewicz, A. Królikowska and P. Wróbel, *ACS Appl. Mater. Interfaces*, 2025, **17**, 23076–23093.
153 Y.-L. Li, J. Zhu, G.-J. Weng, J.-J. Li, X. Li and J.-W. Zhao, *Sens. Actuators, B*, 2025, **442**, 138115.
154 X. Wu, S. Ding, J. Sun, S. Li, R. Fan, Z. Wu and K. Wu, *ACS Appl. Mater. Interfaces*, 2025, **17**, 52463–52473.
155 A. Otto, A. Bruckbauer and Y. X. Chen, *J. Mol. Struct.*, 2003, **661–662**, 501–514.
156 S. E. J. Bell and N. M. S. Sirimuthu, *J. Am. Chem. Soc.*, 2006, **128**, 15580–15581.
157 D. J. Anderson and M. Moskovits, *J. Phys. Chem. B*, 2006, **110**, 13722–13727.
158 S. J. Lee, A. R. Morrill and M. Moskovits, *J. Am. Chem. Soc.*, 2006, **128**, 2200–2201.
159 G. Braun, I. Pavel, A. R. Morrill, D. S. Seferos, G. C. Bazan, N. O. Reich and M. Moskovits, *J. Am. Chem. Soc.*, 2007, **129**, 7760–7761.
160 B. Vlčková, M. Moskovits, I. Pavel, K. Šišková, M. Sládková and M. Šlouf, *Chem. Phys. Lett.*, 2008, **455**, 131–134.
161 L. Fabris, M. Dante, T.-Q. Nguyen, J. B.-H. Tok and G. C. Bazan, *Adv. Funct. Mater.*, 2008, **18**, 2518–2525.
162 S. J. Tan, M. J. Campolongo, D. Luo and W. Cheng, *Nat. Nanotechnol.*, 2011, **6**, 268–276.
163 M. M. Maye, D. Nykypanchuk, M. Cuisinier, D. van der Lelie and O. Gang, *Nat. Mater.*, 2009, **8**, 388–391.
164 M. M. Maye, M. T. Kumara, D. Nykypanchuk, W. B. Sherman and O. Gang, *Nat. Nanotechnol.*, 2010, **5**, 116–120.
165 D. Graham, D. G. Thompson, W. E. Smith and K. Faulds, *Nat. Nanotechnol.*, 2008, **3**, 548–551.
166 X. Qian, X. Zhou and S. Nie, *J. Am. Chem. Soc.*, 2008, **130**, 14934–14935.
167 Y. Wang, K. Lee and J. Irudayaraj, *Chem. Commun.*, 2010, **46**, 613–615.
168 Z. Kunushpayeva, A. Rapikov, A. Akhmetova, A. Sultangaziyev, D. Dossym and R. Bukasov, *Sens. Biosens. Res.*, 2020, **29**, 100355.
169 H. Kang, S. Jeong, J.-K. Yang, A. Jo, H. Lee, E. H. Heo, D. H. Jeong, B.-H. Jun, H. Chang and Y.-S. Lee, *Int. J. Mol. Sci.*, 2021, **22**, 1752.
170 B. A. Junisu and Y.-S. Sun, *ACS Appl. Nano Mater.*, 2020, **3**, 7950–7962.
171 B. Lin, P. Kannan, B. Qiu, Z. Lin and L. Guo, *Food Chem.*, 2020, **307**, 125528.
172 C. Zhu, G. Meng, P. Zheng, Q. Huang, Z. Li, X. Hu, X. Wang, Z. Huang, F. Li and N. Wu, *Adv. Mater.*, 2016, **28**, 4871–4876.
173 D. Huo, B. Chen, M. Li, G. Meng, Y. Lei and C. Zhu, *Nanotechnology*, 2021, **32**, 145302.
174 S. Chinnakkannu Vijayakumar, K. Venkatakrishnan and B. Tan, *ACS Appl. Mater. Interfaces*, 2017, **9**, 5077–5091.
175 K. Karn-orachai, Y. Sanguansap, K. Pankleaub, O. Noppha, N. Wiriyakun, P. Kanatharana and R. laocharoensuk, *Appl. Surf. Sci.*, 2020, **529**, 147236.
176 P. Wen, F. Yang, C. Ge, S. Li, Y. Xu and L. Chen, *Nanotechnology*, 2021, **32**, 395502.
177 R. M. Jarvis and R. Goodacre, *Chem. Soc. Rev.*, 2008, **37**, 931–936.
178 Y. Cao, J. Zhang, Y. Yang, Z. Huang, N. V. Long and C. Fu, *Appl. Spectrosc. Rev.*, 2015, **50**, 499–525.
179 X. X. Han, Y. Ozaki and B. Zhao, *TrAC, Trends Anal. Chem.*, 2012, **38**, 67–78.
180 Y. Wang and J. Irudayaraj, *Philos. Trans. R. Soc., B*, 2013, **368**, 20120026.
181 S. Tian, O. Neumann, M. J. McClain, X. Yang, L. Zhou, C. Zhang, P. Nordlander and N. J. Halas, *Nano Lett.*, 2017, **17**, 5071–5077.
182 U. S. Dinish, F. C. Yaw, A. Agarwal and M. Olivo, *Biosens. Bioelectron.*, 2011, **26**, 1987–1992.
183 Y. Zhang, C. Li, Z. Fakhraai, B. Moosa, P. Yang and N. M. Khashab, *ACS Omega*, 2018, **3**, 14399–14405.
184 Y. Wang, K. Lee and J. Irudayaraj, *J. Phys. Chem. C*, 2010, **114**, 16122–16128.
185 E. Witkowska, D. Korsak, A. Kowalska, A. Janeczek and A. Kamińska, *Anal. Bioanal. Chem.*, 2018, **410**, 5019–5031.
186 T. M.-H. Lee, *Sensors*, 2008, **8**, 5535–5559.
187 W. Zhou, Y.-F. Tian, B.-C. Yin and B.-C. Ye, *Anal. Chem.*, 2017, **89**, 6120–6128.
188 B. Guven, F. C. Dudak, I. H. Boyaci, U. Tamer and M. Ozsoz, *Analyst*, 2014, **139**, 1141–1147.
189 T. Kang, S. M. Yoo, I. Yoon, S. Y. Lee and B. Kim, *Nano Lett.*, 2010, **10**, 1189–1193.
190 Y. Zhou, W. Fang, K. Lai, Y. Zhu, X. Bian, J. Shen, Q. Li, L. Wang, W. Zhang and J. Yan, *Biosens. Bioelectron.*, 2019, **141**, 111419.
191 G. Wang, R. J. Lipert, M. Jain, S. Kaur, S. Chakraboty, M. P. Torres, S. K. Batra, R. E. Brand and M. D. Porter, *Anal. Chem.*, 2011, **83**, 2554–2561.
192 X. Terzapulo, A. Kassenova and R. Bukasov, *Int. J. Mol. Sci.*, 2024, **25**, 2080.
193 R. Bukasov, A. Sultangaziyev, Z. Kunushpayeva, A. Rapikov and D. Dossym, *Int. J. Mol. Sci.*, 2023, **24**, 5578.
194 S. Mergenbayeva, X. Terzapulo and R. Bukasov, *Molecules*, 2025, **30**, 3974.
195 A. Ilyas, A. Dyussupova, A. Sultangaziyev, Y. Shevchenko, O. Filchakova and R. Bukasov, *Talanta*, 2023, **265**, 124818.
196 L. Xu, W. Yan, W. Ma, H. Kuang, X. Wu, L. Liu, Y. Zhao, L. Wang and C. Xu, *Adv. Mater.*, 2015, **27**, 1706–1711.
197 K. H. Drexhage, H. Kuhn and F. P. Schäfer, *Ber. Bunsenges. Phys. Chem.*, 1968, **72**, 329.
198 K. H. Drexhage, *J. Lumin.*, 1970, **1–2**, 693–701.
199 J. R. Lakowicz, *Anal. Biochem.*, 2001, **298**, 1–24.
200 D. G. Chris, G. Ignacy, M. Joanna, G. Zygmunt and R. L. Joseph, *Comb. Chem. High Throughput Screening*, 2003, **6**, 109–117.
201 K. Aslan, J. R. Lakowicz, H. Szmacinski and C. D. Geddes, *J. Fluoresc.*, 2004, **14**, 677–679.
202 K. Aslan, I. Gryczynski, J. Malicka, E. Matveeva, J. R. Lakowicz and C. D. Geddes, *Curr. Opin. Biotechnol.*, 2005, **16**, 55–62.
203 T. Schalkhammer, F. Aussenegg, A. Leitner, H. Brunner, G. Hawa, C. Lobmaier and F. Pittner, *Detection of*

Fluorophore-Labeled Antibodies by Surface-Enhanced Fluorescence on Metal Nanoislands, SPIE, 1997.
204 J. R. Lakowicz, B. Shen, Z. Gryczynski, S. D'Auria and I. Gryczynski, *Biochem. Biophys. Res. Commun.*, 2001, **286**, 875–879.
205 F. Tang, F. He, H. Cheng and L. Li, *Langmuir*, 2010, **26**, 11774–11778.
206 H. Li, W. Qiang, M. Vuki, D. Xu and H.-Y. Chen, *Anal. Chem.*, 2011, **83**, 8945–8952.
207 W. Qiang, H. Li and D. Xu, *Anal. Methods*, 2013, **5**, 629–635.
208 S. R. Ahmed, M. A. Hossain, J. Y. Park, S.-H. Kim, D. Lee, T. Suzuki, J. Lee and E. Y. Park, *Biosens. Bioelectron.:X*, 2014, **58**, 33–39.
209 Z. Mei and L. Tang, *Anal. Chem.*, 2017, **89**, 633–639.
210 T. Tian, Y. Zhong, C. Deng, H. Wang, Y. He, Y. Ge and G. Song, *Talanta*, 2017, **162**, 135–142.
211 A. Sultangaziyev and R. Bukasov, *Sens. Biosens. Res.*, 2020, **30**, 100382.
212 S. Pan, Y. Zhu, G. Shi, Z. Shang and M. Wang, *Optik*, 2020, **223**, 165377.
213 A. Bek, R. Jansen, M. Ringler, S. Mayilo, T. A. Klar and J. Feldmann, *Nano Lett.*, 2008, **8**, 485–490.
214 C.-C. Fu, G. Ossato, M. Long, M. A. Digman, A. Gopinathan, L. P. Lee, E. Gratton and M. Khine, *Appl. Phys. Lett.*, 2010, **97**, 203101.
215 R. Gill and E. C. Le Ru, *Phys. Chem. Chem. Phys.*, 2011, **13**, 16366–16372.
216 H. Li, C.-Y. Chen, X. Wei, W. Qiang, Z. Li, Q. Cheng and D. Xu, *Anal. Chem.*, 2012, **84**, 8656–8662.
217 L. Zhou, F. Ding, H. Chen, W. Ding, W. Zhang and S. Y. Chou, *Anal. Chem.*, 2012, **84**, 4489–4495.
218 Y. Fu, J. Zhang and J. R. Lakowicz, *Langmuir*, 2013, **29**, 2731–2738.
219 D. Punj, M. Mivelle, S. B. Moparthi, T. S. van Zanten, H. Rigneault, N. F. van Hulst, M. F. García-Parajó and J. Wenger, *Nat. Nanotechnol.*, 2013, **8**, 512–516.
220 T. Kinoshita, D. Q. Nguyen, T. Nishino, H. Nakao, H. Shiigi and T. Nagaoka, *Anal. Sci.*, 2015, **31**, 487–493.
221 T. Zhang, N. Gao, S. Li, M. J. Lang and Q.-H. Xu, *J. Phys. Chem. Lett.*, 2015, **6**, 2043–2049.
222 R. Regmi, J. Berthelot, P. M. Winkler, M. Mivelle, J. Proust, F. Bedu, I. Ozerov, T. Begou, J. Lumeau, H. Rigneault, M. F. Garcia-Parajo, S. Bidault, J. Wenger and N. Bonod, *Nano Lett.*, 2016, **16**, 5143–5151.
223 V. Flauraud, R. Regmi, P. M. Winkler, D. T. L. Alexander, H. Rigneault, N. F. van Hulst, M. F. Garcia-Parajo, J. Wenger and J. Brugger, *Nano Lett.*, 2017, **17**, 1703–1710.
224 E. Hohenberger, N. Freitag, D. Rosenmann and V. Korampally, *Sens. Actuators, B*, 2017, **249**, 549–557.
225 H. Yanagawa, T. Hinamoto, T. Kanno, H. Sugimoto, M. Shioi and M. Fujii, *J. Appl. Phys.*, 2019, **126**, 223104.
226 Z. Shang, M. Wang, S. Pan, X. Sun, G. Shi, X. Yan, W. Ma and T. Jiao, *Opt. Commun.*, 2019, **451**, 345–352.
227 J. S. Pang, I. G. Theodorou, A. Centeno, P. K. Petrov, N. M. Alford, M. P. Ryan and F. Xie, *ACS Appl. Mater. Interfaces*, 2019, **11**, 23083–23092.
228 Y. Wei, H. Pei and Q. Dai, *Optik*, 2020, **217**, 164883.
229 J. Dong, F. Wu, Q. Han, J. Qi, W. Gao, Y. Wang, T. Li, Y. Yang and M. Sun, *RSC Adv.*, 2020, **10**, 36042–36050.
230 D. F. Cruz, C. M. Fontes, D. Semeniak, J. Huang, A. Hucknall, A. Chilkoti and M. H. Mikkelsen, *Nano Lett.*, 2020, **20**, 4330–4336.
231 J. Kim, N. Abbas, S. Lee, J. Yeom, A. M. Asgar, M. A. Badshah, X. Lu, Y. K. Kim and S.-M. Kim, *Polymers*, 2021, **13**, 48.
232 X. Lu, S. Lee, J. Kim, N. Abbas, M. A. Badshah and S.-m. Kim, *Biosens. Bioelectron.*, 2021, **175**, 112881.
233 J.-M. Kim, C. Lee, Y. Lee, J. Lee, S.-J. Park, S. Park and J.-M. Nam, *Adv. Mater.*, 2021, **33**, 2006966.
234 P. Roy, S. Zhu, J.-B. Claude, J. Liu and J. Wenger, *ACS Nano*, 2023, **17**, 22418–22429.
235 J. Wang, Q. Hao, H. Dong, M. Zhu, L. Wu, L. Liu, W. Wang, O. G. Schmidt and L. Ma, *Nanoscale*, 2023, **15**, 1128–1135.
236 W. Deng, F. Xie, H. T. M. C. M. Baltar and E. M. Goldys, *Phys. Chem. Chem. Phys.*, 2013, **15**, 15695–15708.
237 R. Bukasov, O. Filchakova, K. Gudun and M. Bouhrara, *J. Fluoresc.*, 2017, **28**, 1–4.
238 A. Sultangaziyev, A. Akhmetova, Z. Kunushpayeva, A. Rapikov, O. Filchakova and R. Bukasov, *Sens. Biosens. Res.*, 2020, **28**, 100332.
239 R. Bukasov, Z. Kunushpayeva, A. Rapikov, S. Zhunussova, A. Sultangaziyev and O. Filchakova, *J. Fluoresc.*, 2020, **30**, 1477–1482.
240 M. H. Chowdhury, K. Ray, S. K. Gray, J. Pond and J. R. Lakowicz, *Anal. Chem.*, 2009, **81**, 1397–1403.
241 S. Wang, B. Li, J. Xiang, L. Li, S. Xi, R. Pan, Z. Luan, L. Chen and X. Zhang, *TrAC, Trends Anal. Chem.*, 2025, **191**, 118353.
242 A.-S. Tatar, S. Boca, A. Falamas, D. Cuibus and C. Farcău, *Analyst*, 2023, **148**, 3992–4001.
243 A. Falamas and C. Farcău, *Methods Appl. Fluoresc.*, 2025, **13**, 035003.